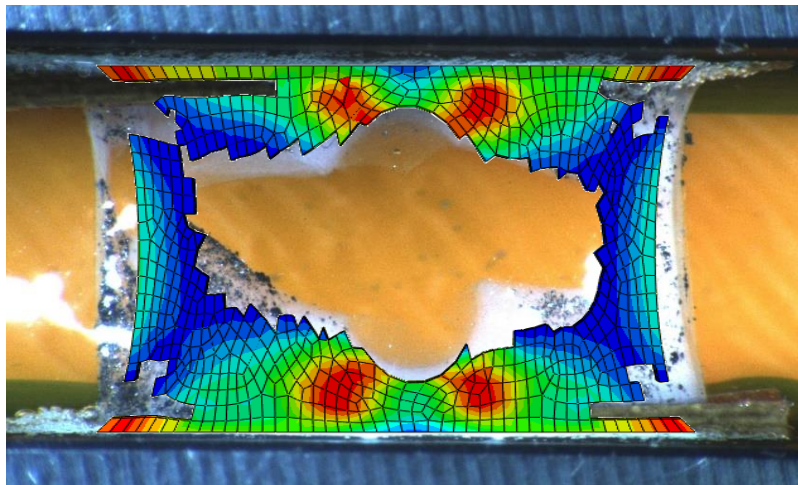


A Strain Energy Limiter Approach for Atherosclerotic Plaque Rupture Modelling

Aikaterini Tziotziou

MSc Thesis

Biomedical Engineering



A Strain Energy Limiter Approach for Atherosclerotic Plaque Rupture Modelling

By

Aikaterini Tziotziou

in partial fulfilment of the requirements for the degree of

Master of Science

at the Delft University of Technology,

to be defended publicly on Thursday December 3, 2020 at 10:00 AM.

Student Number: 4906403

Supervisors: Dr. ir. Ali C. Akyildiz (Erasmus MC)

Dr. ir. Lidy Fratila-Apachitei (TU Delft)

Prof. Dr. ir. Amir A. Zadpoor (TU Delft)

An electronic version of this thesis is available at <http://repository.tudelft.nl/>.



Acknowledgements

I would like to thank my daily supervisor at Erasmus MC, Dr. ir. Ali C. Akyildiz who always supported and guided me during my Master Thesis. He was my inspiring mentor with constant motivation to explore new strategies of simulating the plaque rupture mechanism. I am grateful for this cooperation as I gained a lot of educative and precious knowledge. I would like to thank Tamar Wissing and Sheila Serra for providing me useful experimental data and brainstorm ideas during our meetings. In addition, I would like to thank my TU Delft supervisor, Dr. ir. E.L. Fratila-Apachitei who successfully guided and encouraged me through my Graduation Project.

I would like to thank my colleagues in the Cardiovascular Biomechanics Laboratory – Thoraxcenter of Erasmus MC for this unique opportunity. I am glad to be part of this innovative and multidiscipline team including Engineers, Biologists and Medical Doctors, as they are supportive and experienced scientists that helped me throughout my Master Thesis Project.

Contents

Abstract.....	12
1. Introduction.....	12
2. Materials and Methods.....	13
2.1 Constitutive Models of Plaque Tissue.....	14
2.2 Tissue Damage Modeling via Energy Limiter Approach.....	15
2.3 Finite Element Implementation.....	17
2.4 Application to Predict Damage in Plaque-Mimicking Tissue-Engineered Samples.....	17
2.4.1 Experimental Rupture Data.....	17
2.4.2 Computational Models.....	18
2.5 Parametric Study of SEDF with different and varying Energy Limiters for the matrix and the fibrous components.....	20
3. Results.....	21
3.1 Qualitative comparison.....	21
3.2 Quantitative Assessment.....	23
3.3 Parametric Study Results.....	25
4. Discussion.....	26
5. Conclusion.....	27
Appendix A.1.....	30
Appendix A.2.....	33
Appendix A.3.....	35
Appendix B.....	36
Appendix C.....	41
Appendix D.....	41
Appendix E.....	46

List of Figures

Fig. 1. The effect of $\beta_k \in [-1, 1]$ parameter of the SEDF with energy limiter damage model on the damage evolution of the factor D when $\Xi_{\min} < \Xi < \Xi_{\max}$. The “ $\beta_k=0$ ” curve represents a more linear damage evolution from Ξ_{\min} to Ξ_{\max} ([Oliviera et al., 2016, p.2](#)).....16

Fig.2. Experimental data from atherosclerotic plaque-mimicking tissue-engineered samples with dog bone or rectangular shape. Collagen fibers were incorporated within the tissue and the lipid pool was depicted by a soft inclusion in the middle. The plaque samples were attached in Velcro constructs for uniaxial stretching17

Fig.3. The real test sample (left) and the corresponding ABAQUS computational models: “Ideal” (mid) and “Image-based” (right).....18

Fig. 4. The load-displacement curves of Mesh 1, Mesh 2 and Mesh 3 cases during the mesh convergence analysis. The curve of Mesh 1 (coarse mesh) presented the highest deviation from Mesh 2 and Mesh 3 results.....19

Fig. 5. The experimental force-displacement curve of a test sample (Sample #6). The crack initiation was assumed to be at the maximum force (point B). The region A – B was identified as “no-damage” and the region B – C as “damaged”20

Fig.6. A representative example case of qualitative crack initiation and propagation comparison between experimental data and HGO with zero κ value computational simulations following the SEDF with energy limiter damage model. The variables SDV7, 8 illustrated the SEDF in MPa.....22

Fig. 7. Experimental and computational results of the tissue sample #6 regarding the Maximum Principal Cauchy Stress vs Logarithmic strain data.....23

Fig. 8. Experimental and computational results of the tissue sample #6 regarding the SEDF with energy limiter vs simulation Time data.....24

Fig. 9. 8 curves of tissue SEDF with energy limiter vs simulation time regarding all crack initiation threshold combinations between matrix and fibrous components at 20%, 40%, 60% and 80% of total time.....28

Fig.10. Flowchart of all required steps during the HGO material parameters estimation via a developed iterative optimization.....37

Fig. 11. The Cauchy stress values of all 20 displacement cases regarding the experimental data and the HGO material model with $\kappa = 0$ and 0.333 after the iterative optimization procedure.....40

Fig. 12. Quantitative comparison of Maximum Principal Cauchy Stress vs Logarithmic Strain of the first damaged element between experimental data and computational models following the SEDF with energy limiter damage model.....46

Fig. 13. Quantitative comparison of Strain Energy Density Function with energy limiter vs Time of the first damaged element between computational models of Neo-Hookean and HGO.....47

List of Tables

Table 1. The geometrical dimensions of length, width in the middle section of four dog-bone and four rectangular shapes, average thickness and the applied displacement regarding the eight tissue ruptured cases.....	18
Table 2. The crack initiation thresholds in the HGO model set at 20%, 40%, 60% and 80% of the total analysis time regarding the matrix and fibres components. The energy thresholds were calculated according to the UMAT code presented in Appendix C	21
Table 3. The numerical calculations of Cauchy stress and Elasticity tensor of Neo Hooken and HGO material models (Fehervary et al., 2020 ; Nolan et al., 2020).....	30
Table 4. The verification procedure of HGO UMAT code regarding 12 different loading conditions in all directions.....	33
Table 5. Implementation of energy limiter in UMAT written in Fortran for Neo-Hookean and HGO material models.....	35
Table 6. The separate matrix and fibers SEDF with energy limiter calculations and reduction factors via HGO UMAT code.....	41
Table 7. Crack initiation comparison between experimental data and Ideal computational models, where variable SDV7,8 is the Strain Energy Density Function with energy limiter distribution.....	42
Table 8. Crack initiation comparison between experimental data and Image-based computational models, where variable SDV7,8 is the Strain Energy Density Function with energy limiter distribution.....	43
Table 9. Crack propagation comparison between experimental data and Ideal computational models, where variable SDV7,8 is the Strain Energy Density Function with energy limiter distribution.....	44
Table 10. Crack propagation comparison between experimental data and Image- based computational models, where variable SDV7,8 is the Strain Energy Density Function with energy limiter distribution.....	45

“A Strain Energy Limiter Approach for Atherosclerotic Plaque Rupture Modelling”

Abstract- Atherosclerosis is a prevalent cardiovascular disease and defined as plaque formation inside the arterial intima layer. The atherosclerotic plaque is characterized as anisotropic, soft tissue and a potential plaque rupture could result in life-threatening clinical events, such as ischemic attack or stroke. The plaque rupture mechanism is still poorly understood due to the lack of real-time, in-vivo observations. Aiming to predict and describe the plaque damage behavior, numerical damage models have been implemented. This study focused on developing a theoretical and computational framework of Strain Energy Density Function (SEDF) with energy limiter damage model with atherosclerotic plaque-mimicking tissue-engineered applications. The generated damage model was implemented in Neo-Hookean and Holzapfel-Gasser-Ogden (HGO) SEDF via material user subroutines (UMAT codes) in finite element software. The computational models simulated 8 different experimental ruptured cases based on idealized and realistic geometrical models. In the material characterization process an iterative optimization algorithm was developed. The findings demonstrated that the case-specific computational models with SEDF with energy limiter damage model reproduced the plaque-mimicking rupture as they fitted the experimental crack initiation and propagation patterns. The results revealed that the anisotropic HGO material model generated the highest amount of Cauchy stresses and strain energy density. In addition, the geometrical configuration sensitivity of the damage model was emphasized as all cracks initiated from the inclusion and the results between idealized and realistic geometrical models deviated. A parametric study was conducted to investigate the influence of various energy limiters in matrix and fibers components via the SEDF and resulted in a matrix-dominated damage model. The SEDF with energy limiter model could be further optimized by developing a fully automated damage model and validated with clinical applications.

Keywords: Atherosclerosis – Plaque – Computational – Numerical – Strain Energy Density Function – Energy Limiter – Damage – UMAT.

1. Introduction

Atherosclerosis is one of the most widespread diseases in human cardiovascular system and a primary cause of death as it can lead to myocardial attack or stroke. It is usually a progressive disease and takes decades for full-symptom development. But the blockage of the arterial lumen can be instantaneous with hazardous outcome if an atherosclerotic lesion site in an artery, namely atherosclerotic plaque, ruptures. In the US approximately 610,000 people annually succumb to heart disease and that equals to 1 out of every 4 deaths. Specifically, 75% of heart attacks occur from plaque rupture every year ([Virmani et al., 2008](#); [Pahwa et al., 2020](#)).

Atherosclerotic plaque rupture triggers a thrombotic cascade, where eventually a blood clot is formed, completely or partially occluding a vessel leading to life-threatening events. The plaque rupture behavior could be mechanically characterized as material fracture based on the accumulation of imperfections like voids and cracks at micro-level followed by irreversible and heterogeneous effects that form cracks at macro-level. Material fracture could be divided into two parts: the crack initiation and the crack propagation but the mechanism(s) in either phenomena is scientifically not well studied for atherosclerotic plaque rupture yet. The greatest challenge involved arises as in-vivo, real-time observations and measurements of plaque tissue rupture are hard to make. Alternative is utilizing numerical damage models in order to describe and predict the fracture mechanism of atherosclerotic plaque tissue ([Holzapfel et al., 2014](#); [Gultekin et al., 2016](#)).

Although limited in number, some computational models have been developed to study the atherosclerotic plaque and arterial damage. In the studies of Gasser et al., Badel et al. and Leng et al. a cohesive zone modelling (CZM) method was used, as a numerical atherosclerotic plaque damage

model, in order to depict the local delamination process between the plaque and the arterial wall during stent deployment illustrating a “smooth” and continuous damage evolution from the stiffening into the softening effect during failure process. The atherosclerotic plaque rupture was also simulated via CZM technique by Ferrara et al., with gradual surface separation within the defined crack tip, based on traction-separation law and material degradation ([Gasser et al., 2007](#); [Ferrara et al., 2008](#); [Badel et al., 2014](#); [Leng et al., 2015](#)). However, the application of CZM method introduced some limitations as the cohesive zone elements are usually isotropic with linear, elastic mechanical response precluding the anisotropic failure mechanism. The studies of Versluis et al., Pei et al. and Huang et al. considered the damage in plaque as a consequence of a fatigue mechanism owing to the fact that inside the arteries the blood pressure follows a cyclic loading pattern which can potentially lead to deterioration of plaque tissue ([Versluis et al., 2006](#); [Pei et al., 2013](#); [Huang et al., 2013](#)). Fatigue damage models regarding engineering materials are based on the fact that the geometrical or structural configuration of the model is preserved during the fatigue process but for biological tissues, like atherosclerotic plaque, the applicability of this approach is questionable as the tissues may remodel and change their structure over time.

In the framework of continuum mechanics, soft biological tissues like atherosclerotic plaque demonstrate anisotropic mechanical responses under large deformations they physiologically undergo due to their structural composition (matrix and fibers components). Their constitutive behavior is commonly prescribed with a Strain Energy Density Function (SEDF) from which stress–strain relations and elasticity tensors can be obtained ([Simo, 1987](#); [Calvo et al., 2006](#); [Rodriguez et al., 2008](#); [Pena et al., 2011](#); [Saez et al., 2012](#)). Damage can be implemented in SEDF by energy limiter approach including information regarding the high complexity between the fibers and matrix components and describe the procedures occurring within the tissue during the failure process. The main benefit of SEDF with energy limiter compared to other discontinuous fracture mechanisms is the representation of the anisotropic, inelastic and non-linear fracture behavior of a soft tissue and its great adaptability regarding multiple hyper-elastic material models and damage mechanisms allows modeling the “global” tissue failure. Applications of the SEDF with energy limiter, as a damage model in healthy arterial tissues, are presented in the studies of Volokh et al., Famaey et al., Ferreira et al., Mousavi et al., and Pena et al. combined with experimental validations ([Volokh et al., 2011](#); [Famaey et al., 2013](#); [Ferreira et al., 2013](#); [Mousavi et al., 2018](#); [Pena et al., 2019](#)).

The current study aims developing a theoretical and computational framework of a Strain Energy Density Function (SEDF) with energy limiter damage model to describe an atherosclerotic plaque damage mechanism. To the author’s knowledge, the current study presents for the first time the SEDF with energy limiter as an atherosclerotic plaque damage model. First, a SEDF with energy limiter was proposed, and numerically implemented in a commercial finite element software framework. Then, the developed model was used in case-specific computational simulations of rupture experiments of atherosclerotic plaque-mimicking engineered tissue samples.

2. Materials and Methods

The atherosclerotic plaque is usually modeled as a hyper-elastic, nearly incompressible composite material due to its non-linear mechanical stress-strain response under large deformation and the structural composition ([Holzapfel et al., 2014](#)). In the current study, the computational models of atherosclerotic plaque focused on two SEDF, the Neo-Hookean and the Holzapfel-Gasser-Ogden (HGO) hyper-elastic models, commonly used for atherosclerotic plaques ([Akyildiz et al., 2017](#)). The plaque rupture mechanism was simulated with the commercial finite element software ABAQUS/Standard (Dassault Systems) via the approach of a Strain Energy Density Function (SEDF)

with energy limiter. First, an SEDF with energy limiter was developed, verified and implemented for both material models using material user subroutines (UMAT) written in Fortran. Due to the lack of atherosclerotic plaque rupture test data, the developed damage model was applied in eight recently obtained plaque-mimicking tissue-engineered samples ([Master Thesis Serra, S., 2020](#)) ending up with 48 3D computational models. An additional parametric study was conducted regarding the variation of crack initiation thresholds between matrix and fibres components in order to gain better insight into the damage model of SEDF with multiple energy limiters.

2.1 Constitutive Models of Plaque Tissue

A Strain Energy Density Function (SEDF) defines the stored energy in a material due to the deformation it has undergone by using a hyper-elastic material model. The mechanical response of the material can be then derived from the defined SEDF. The SEDF, Ψ can be split into the volume-preserving, deviatoric part, Ψ_{dev} and the volumetric (or volume-changing) part, Ψ_{vol} , expressed as ([Rodriguez et al., 2008](#); [Volokh, 2011](#)):

$$\Psi = \Psi_{\text{dev}} + \Psi_{\text{vol}}. \quad (1)$$

With respect to the applications to fibrous soft tissues, that consist of a non-collagenous ground matrix with embedded collagen fibers, the deviatoric part Ψ_{dev} can be further decoupled into an isotropic component Ψ_{iso} and an anisotropic component Ψ_{aniso} , reflecting the isotropic influence of the matrix material and the anisotropic contribution of fibres, respectively. Then the corresponding SEDF can be defined as

$$\Psi(\tilde{\mathbf{C}}) = \Psi_{\text{iso}}(\bar{\mathbf{C}}) + \Psi_{\text{ani}}(\bar{\mathbf{C}}) + \Psi_{\text{vol}}(J) \quad (2)$$

where $\tilde{\mathbf{C}}$ is the right Cauchy–Green strain tensor defined as $\tilde{\mathbf{C}} = \mathbf{F}^T \mathbf{F}$, \mathbf{F} is the deformation gradient tensor, $\bar{\mathbf{C}}$ is the deviatoric part of the right Cauchy–Green strain tensor, given as $\bar{\mathbf{C}} = \bar{\mathbf{F}}^T \bar{\mathbf{F}}$, $\bar{\mathbf{F}} = J^{-1/3} \mathbf{F}$ and Jacobian $J = \det(\mathbf{F})$ ([Pena et al., 2007](#)).

Neo-Hookean Material Model

The Neo-Hookean model is commonly implemented in arterial wall and atherosclerotic plaque computational models depicting their non-linear mechanical response ([Akyildiz et al., 2015](#); [Akyildiz et al., 2017](#)). The Neo-Hookean SEDF, Ψ_{NH} is a hyper-elastic material model that provides an isotropic, non-linear behaviour and is given by

$$\Psi_{\text{NH}} = \underbrace{C_{10}(\bar{I}_1 - 3)}_{\Psi_{\text{iso}}(\bar{\mathbf{C}})} + \underbrace{\frac{1}{D_1}(J - 1)^2}_{\Psi_{\text{vol}}(J)}. \quad (3)$$

In the above expression C_{10} is a material constant, $\bar{I}_1 = \text{tr}(\bar{\mathbf{C}})$ is the first invariant of the deviatoric part of the Cauchy-Green deformation tensor and D_1 is the material's incompressibility parameter ([deBotton et al., 2005](#)).

Holzappel-Gasser-Ogden (HGO) Material Model

The HGO material model was originally developed for modeling the fibre-families and the non-collagenous matrix components within the arterial layers (adventitia and intima layer) including the mechanical contribution of both components (isotropy and anisotropy) in the same equation forming a

generic material model. In the HGO model, Ψ_{HGO} more than one fibre-family can be incorporated within the structure and its SEDF is expressed as

$$\Psi_{HGO} = \underbrace{C_{10}(\bar{I}_1 - 3)}_{\Psi_{iso}(\bar{C})} + \underbrace{\frac{1}{D_1} \left[\frac{(J)^2 - 1}{2} - \ln J^{e\ell} \right]}_{\Psi_{vol}(J)} + \underbrace{\frac{k_1}{2k_2} \sum_i^n \left[\exp \left(k_2 \left\langle \kappa(\bar{I}_1 - 3) + (1 - 3\kappa)(\bar{I}_{4(i)} - 1) \right\rangle^2 \right) - 1 \right]}_{\Psi_{ani}(\bar{C})} \quad (4)$$

where k_1 describes the relative stiffness of the fibre families in small strain range, k_2 presents a dimensionless stiffness parameter regarding large strain range, n describes the total number of fiber families, κ ($0 \leq \kappa \leq 1/3$) controls the dispersion rate within the fibre families directions (if $\kappa=0$ the fibers are perfectly aligned in one direction and if $\kappa=1/3$ the fibres are randomly distributed leading to isotropic material behavior), $\bar{I}_{4(i)} = \alpha_i \cdot \bar{C} \alpha_i$ is the pseudo-invariant of the right Cauchy-Green deformation tensor and α_i is the mean direction of the fiber family i and $\langle \cdot \rangle$ is the ‘‘Macauley bracket’’ operator defined as: $\langle x \rangle = 1/2(|x| + x)$ ([Gasser et al., 2006](#); [Gasser et al., 2007](#); [Holzapfel et al., 2014](#))

2.2 Tissue Damage Modeling via Energy Limiter Approach

The damage evolution is introduced in this study via an energy limiter in the SEDF that enables the atherosclerotic plaque rupture modelling. The energy limiter could be characterized as a saturation factor for the SEDF defining the threshold of the maximum amount of energy that could be stored in the material without fracture, named fracture energy and it is usually implemented through the material constitutive equations. Since it is commonly assumed that the material degradation is only related to the maximum distortional energy (deviatoric part) and is independent of the volumetric part, the energy limiter affects only the deviatoric part of the SEDF and is implemented as ([Pena et al., 2007](#); [Rodriguez et al., 2008](#); [Volokh, 2011](#)).

$$\Psi = (1 - D) \cdot \Psi_{dev} + \Psi_{vol} \quad (5)$$

where $D \in [0, 1]$ is a monotonically increasing internal damage parameter reflecting the percentage of the damaged material ($D=0$ describes a healthy tissue without damage initiation and $D=1$ represents a fully separated and totally damaged tissue) and $(1 - D)$ is the reduction factor ([Pena et al., 2011](#)). The development of the damage parameter D is defined by an equation of irreversible damage evolution given by

$$D = \begin{cases} 0, & \text{if } \Xi < \Xi_{min} \\ \xi^2 [1 - \beta_k (\xi^2 - 1)], & \text{if } \Xi_{min} < \Xi < \Xi_{max} \\ 1, & \text{if } \Xi > \Xi_{max} \end{cases} \quad \text{and} \quad \xi = \frac{\Xi - \Xi_{min}}{\Xi_{max} - \Xi_{min}} \quad (6)$$

where $\beta_k \in [-1, 1]$ is a material parameter affecting the curvature of the damage function when $\Xi_{min} < \Xi < \Xi_{max}$, as shown in [Fig. 1](#) and $\Xi_{min}, \Xi_{max} \in [-1, 1]$ are variables related to the strain energies at initial and fully damage state, respectively. The $\Xi \in [-1, 1]$ variable is expressed by

$$\Xi = \max \sqrt{2 \cdot \Psi(\bar{C})} \quad (7)$$

and the following damage criterion ϕ during the loading conditions is fulfilled ([Simo, 1987](#))

$$\varphi = \sqrt{2 \cdot \Psi(\bar{C})} - \Xi \leq 0. \quad (8)$$

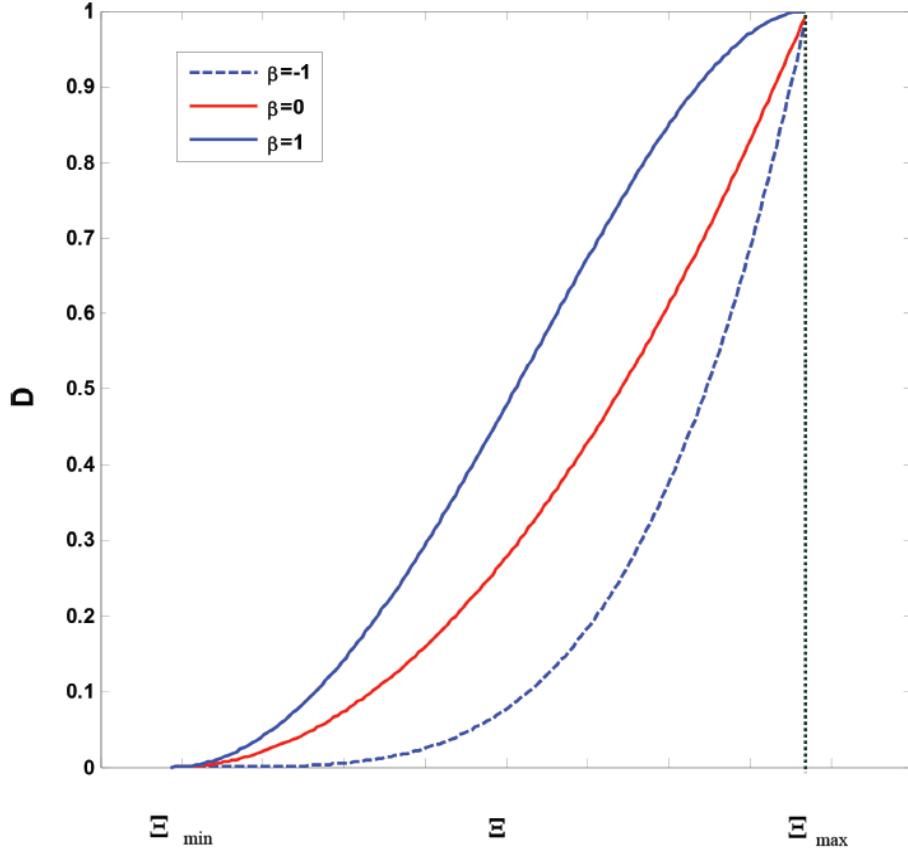


Fig. 1. The effect of $\beta_k \in [-1, 1]$ parameter of the SEDF with energy limiter damage model on the damage evolution of the factor D when $\Xi_{\min} < \Xi < \Xi_{\max}$. The “ $\beta_k=0$ ” curve represents a more linear damage evolution from Ξ_{\min} to Ξ_{\max} (Oliviera et al., 2016, p.2).

The reduction factor $(1 - D)$ influences the mechanical response as it affects the deviatoric part of the Cauchy stress tensor σ_{dev} and the elasticity tensor h_{dev} , defined as:

$$\sigma_{\text{dev}} = (1 - D) \cdot \sigma_{\text{dev}}^0 \quad (9)$$

$$h_{\text{dev}} = (1 - D) \cdot h_{\text{dev}}^0 - D'(\sigma_{\text{dev}}^0 \otimes \sigma_{\text{dev}}^0) \text{ and } D' = 2\xi(1 + \beta_k) - 4\beta_k \xi^3 \text{ if } \Xi_{\min} < \Xi < \Xi_{\max}. \quad (10)$$

Considering that the deviatoric part of the SEDF is further decoupled into the isotropic (matrix component) and the anisotropic part (fiber network), the normalized, scalar, damage variable D could be also separated into the matrix damage parameter ($D_m \in [0, 1]$) and the fibres damage factor ($D_f \in [0, 1]$), given by (Simo, 1987)

$$\Psi(\bar{C}) = (1 - D_m) \cdot \Psi_{\text{iso}}(\bar{C}) + (1 - D_f) \cdot \Psi_{\text{ani}}(\bar{C}) + \Psi_{\text{vol}}(J). \quad (11)$$

The damage evolution of the reduction factors $(1 - D_m)$ and $(1 - D_f)$ are determined by (Calvo et al., 2006)

$$\Xi_m = \sqrt{2 \cdot \Psi_{\text{iso}}(\bar{C})} \text{ and } \Xi_f = \sqrt{2 \cdot \Psi_{\text{ani}}(\bar{C})}. \quad (12)$$

2.3 Finite Element Implementation

The damage development of the reduction factor (1- D) was computationally implemented in the commercial finite element software ABAQUS for the Neo- Hookean and HGO constitutive in order to model the material degradation process. Since the energy limiter approach is not available as a damage model in ABAQUS, the SEDF with energy limiter was developed and implemented through material user subroutines written in Fortran, named UMAT. The numerical development of UMAT codes can be found in [Appendix A.1](#). The verification process of the constitutive models included single-element (C3D8H) models under 12 different loading conditions and a multiple-elements example problem with the model provided by ABAQUS manual (“adventitia_axial.inp”) under tensile testing as described in [Appendix A.2](#). The implementation of the damage loop and the calculation of the “damaged” SEDF and the reduction factor (1- D) in the Neo-Hookean and HGO UMAT codes are provided in [Appendix A.3](#).

2.4 Application to Predict Damage in Plaque-Mimicking Tissue-Engineered Samples

2.4.1 Experimental Rupture Data

Due to the lack of the available rupture data from real atherosclerotic plaque tissue, the developed SEDF with energy limiter was applied for the rupture data set of atherosclerotic plaque-mimicking tissue-engineered samples. The available experimental data was obtained recently in our research group ([Master Thesis Serra, S., 2020](#)). Briefly, the tissue-engineered plaque constructs were generated by culturing isolated human myoblast cells derived from the vena saphena magna with incorporated collagen fiber families. The tissue-engineered scaffolds had a dog-bone or rectangular shape with a soft gel inclusion in the center representing the lipid pool of an atherosclerotic plaque tissue (diameter of 2 mm), as shown in [Fig.2](#).

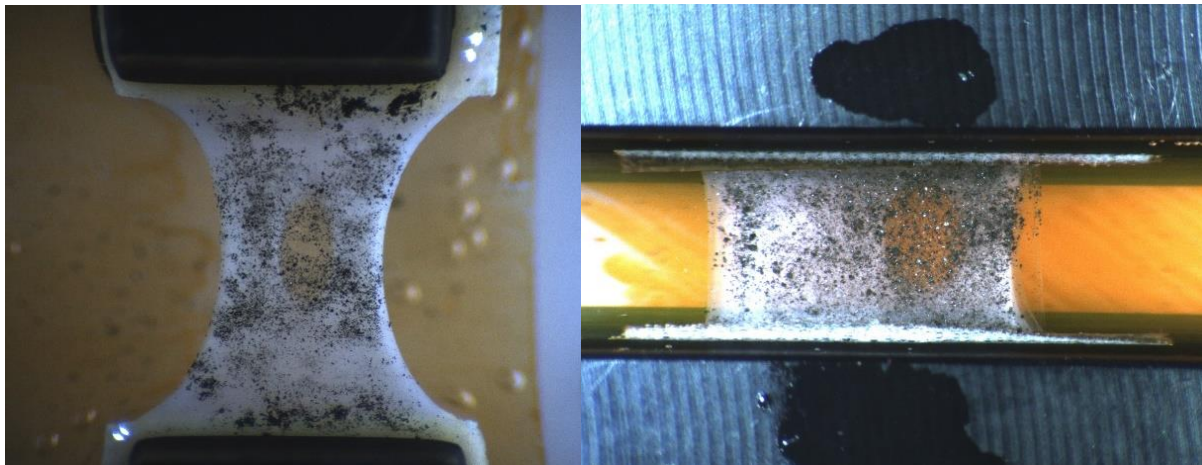


Fig.2. Experimental data from atherosclerotic plaque-mimicking tissue-engineered samples with dog-bone or rectangular shape. Collagen fibers were incorporated within the tissue and the lipid pool was depicted by a soft inclusion in the middle. The plaque samples were attached in Velcro constructs for uniaxial stretching.

Once the samples were cultured and created, they were mechanically tested under uniaxial stretch loading condition until rupture. Eventually, eight tissue samples, out of 42 experimental cases, had a rupture in the central region, next to the soft inclusion. In the present study the rupture tests of these samples were simulated. The geometrical dimensions, such as length, width in the central part of dog-bone or rectangular shape and average thickness of the test samples are presented in [Table 1](#) ([Master Thesis Serra, S., 2020](#)).

Table 1. The geometrical dimensions of length, width in the middle section of four dog-bone and four rectangular shapes, average thickness and the applied displacement regarding the eight tissue ruptured cases.

Sample	Length (mm)	Width (mm)	Average Thickness (mm)	Applied Displacement (mm)
1	4.403	12	0.60	3.667
2	4.828	12	0.65	4.407
3	6.727	5	0.60	4.826
4	8.839	4.5	0.50	2.931
5	9.035	5	0.40	3.969
6	6.541	8.5	0.50	3.355
7	5.557	8	0.55	3.417
8	7.323	5.8	0.35	5.010

2.4.2 Computational Models

The sample-specific computational models of the eight plaque-mimicking engineered-tissue samples were created to simulate the tissue rupture that occurred in the uniaxial tensile testing. In the models, the sample-specific geometry, mechanical behavior and test-specific boundary conditions were incorporated. With respect to the experimental dimension measurements of every ruptured case, first a 3D “Ideal” computational model was created based on the length, width and average thickness measurements but via idealized and symmetrical dog-bone or rectangular shapes including elliptical inclusions in the centre of the tissue.

To investigate any effect of irregular shapes of the experimental tissue samples, a second geometrical model was created for each sample, the “Image-based” models. The 3D “Image-based” geometries followed the exact length and width of the samples as every cross-sectional image was imported as a sketch in ABAQUS 2016 with averaged thickness applied. A representative example (Sample #2) is illustrated in [Fig.3](#). The soft inclusion in the center of the tissue was modeled as a void due to its minimal mechanical contribution.

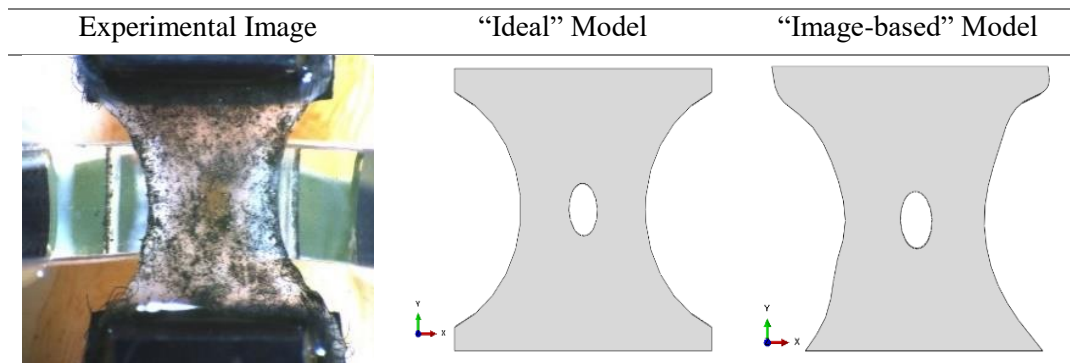


Fig.3. The real test sample (left) and the corresponding ABAQUS computational models: “Ideal” (mid) and “Image-based” (right)

The sample-specific finite element simulations involved uniaxial stretching of the samples along the length direction by test specific displacement boundary condition. Eight-node linear, hybrid elements with reduced integration and enhanced hourglass control with one Gauss point (C3D8RH) were used in the models. During the mesh convergence analysis, Mesh 1 consisted of approximately 8100 elements and 11000 nodes, as a coarse mesh, Mesh 2 was refined as each element edge length was half, in all directions compared to Mesh 1, ending up in about 64000 elements and 76000 nodes and finally Mesh 3 as a stricter mesh refinement analysis with further division of the element dimensions resulted in roughly 235000 elements and 353000 nodes. According to the load-displacement curves of all 3 Mesh categories, as shown in [Fig 4](#), Mesh 2 and Mesh 3 presented similar outcome with average relative error

of all data points 6.6%. Mesh 2 provided well-converged solutions and all computational model results generated from Mesh 2.

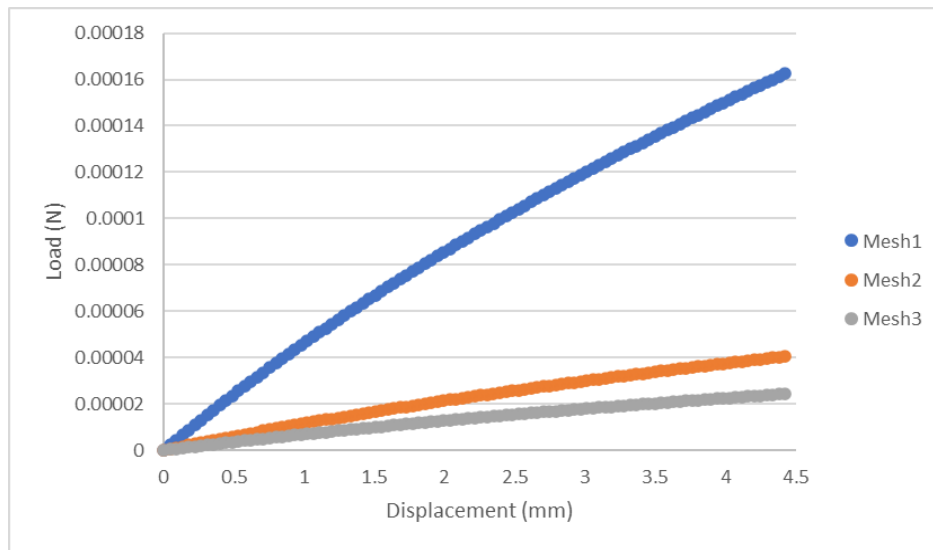


Fig. 4. The load- displacement curves of Mesh 1, Mesh 2 and Mesh 3 cases during the mesh convergence analysis. The curve of Mesh 1 (coarse mesh) presented the highest deviation from Mesh 2 and Mesh 3 results.

In the HGO material models, due to the lack of the structural information of the samples, one fibre family was assumed with the predominant fiber orientation along the length direction and the κ value was set zero (fibres were fully aligned and activated in loading direction) in a set of models and 0.333 (randomly distributed fibres) in another one in order to investigate the influence of the fibre distribution. Consequently, six computational models per sample (“ideal” – “image-based” geometrical and Neo-Hookean – HGO with $\kappa=0$ and $\kappa= 0.333$ material categories) and 48 models in total were simulated.

As the material properties of the plaque-mimicking tissue-engineered samples were not available, a material characterization procedure had to be performed. The material properties of the samples were estimated from the tensile test data of a sample, not included in the sample group analyzed for rupture, without the soft inclusion. It was assumed that all 8 tissue samples have the same properties as they were created following the same culturing protocol.

The Neo-Hookean material properties $C_{10} = 3.0126$ kPa and $D_1 = 1 \cdot e^{-6}$ were obtained by the fully automated inverse identification procedure of ABAQUS 2016 from the engineering (nominal) stress and strain experimental data with average relative error 13%. Since the material evaluation process in ABAQUS is only available for isotropic material models, regarding the HGO model an iterative optimization algorithm was developed through MATLAB R2019a (MathWorks) and Wolfram Mathematica Notebook 12.0.0.0. The details of the procedure can be found in [Appendix B](#). Briefly, the unknown parameter values of the HGO material model, namely C_{10} , k_1 , k_2 and κ were obtained by using 20 experimentally measured pairs of Cauchy stress and displacement data. The tissue was assumed nearly incompressible, hence D_1 value was set $1 \cdot e^{-6}$. An overdetermined system of 20 equations was solved for the material evaluation where the deformation gradient, the left Cauchy deformation tensor, the first and forth invariants were calculated. During the material evaluation a non-linear, curve-fitting, optimization method was implemented, by utilizing the “Trust-Region-Reflective” as least-squares method in MATLAB R2019a (MathWorks) ([Badel et al., 2011](#); [Hajhashemkhani et al., 2015](#)). The estimated HGO material parameters in the case of HGO_{iso} ($\kappa= 0.3333$) were $C_{10} = 2.9$ kPa, $k_1 = 0.0032$ kPa, $k_2 = 0.004$ (average relative error 20%) and in the case of HGO_{aniso} ($\kappa= 0$) the values were $C_{10} = 2.6$ kPa, $k_1 = 0.0028$ kPa, $k_2 = 0.004$ (average relative error 29%).

In the computational analysis of the 48 finite element models, the SEDF was calculated for every element, increment and timeframe based on the implemented UMAT codes. The region from zero (A) to maximum (B) experimental force was assumed without damage as during this time the matrix and fibers were fully activated and could bear the uniaxial loading conditions. However, the region from maximum (B) to zero (C) experimental force was assumed to be the “damage” part of the curve where the energy limiter was implemented. To separate the “no-damage” (A – B) and “damage” (B – C) region, the crack initiation threshold was set at the maximum experimental force (B) and the corresponding displacement, as illustrated in [Fig. 5](#).

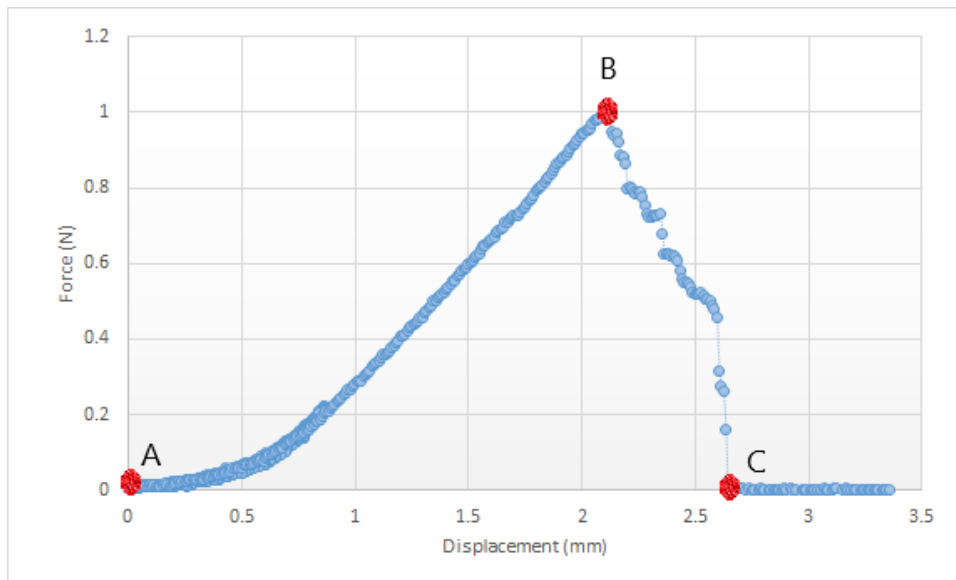


Fig. 5. The experimental force-displacement curve of a test sample (Sample #6). The crack initiation was assumed to be at the maximum force (point B). The region A – B was identified as “no-damage” and the region B – C as “damaged”.

2.5 Parametric Study of SEDF with different and varying Energy Limiters for the matrix and the fibrous components

In previous sections, it was assumed that the matrix and the fibrous components of the HGO models had the same energy limiter threshold. Since it was not clear from the experimental data, if the matrix and the fibrous components had the same or different crack initiation thresholds, a parametric study was conducted in order to investigate the influence of multiple energy limiter thresholds in SEDF of the HGO models.

During the parametric analysis, an “Ideal” dog-bone model was simulated (Sample #2), where the material properties, boundary and mesh conditions followed the protocol described in previous sections. In addition, the damage model in HGO UMAT was revised in order to separate the matrix and the fibrous component SEDFs with energy limiter calculations and their reduction factors ([Appendix C](#)).

The implemented energy thresholds were calculated according to [Eq. 12](#) and the initial (point A in [Fig. 5](#)) and fully damaged (point C in [Fig. 5](#)) thresholds were constant for all case scenarios with values of 0 and 0.065 MPa, respectively. The only parameter that was varied was the crack initiation threshold (point B in [Fig. 5](#)), which was calculated and set at 20%, 40%, 60% and 80% of the total analysis time for the matrix and fibres components separately as depicted in [Table 2](#).

Table 2. The crack initiation thresholds in the HGO model set at 20%, 40%, 60% and 80% of the total analysis time regarding the matrix and fibres components. The energy thresholds were calculated according to the UMAT code presented in [Appendix C](#).

Matrix Crack Initiation Threshold (MPa)	Fibres Crack Initiation Threshold (MPa)
20%: 16.32×10^{-3}	20%: 61.43×10^{-6}
40%: 31.25×10^{-3}	40%: 12.94×10^{-5}
60%: 45.93×10^{-3}	60%: 20.82×10^{-5}
80%: 56.86×10^{-3}	80%: 27.52×10^{-5}

3. Results

The results of the “ideal” (n=24) and “image-based” (n=24) computational models were qualitatively compared with the experimental data regarding the localization of damage (crack initiation point and propagation pattern). A quantitative comparison between Neo-Hookean and HGO material models regarding the maximum principal Cauchy stress and the strain energy density distribution is presented. The effect of multiple energy limiters in matrix and fibrous components on damage initiation and evolution is provided in the results of the parametric study highlighting the influence of a matrix-dominated damage model.

3.1 Qualitative comparison

The qualitative comparison of the computational results to the experimental observations revealed that the crack initiation locations and the crack propagation patterns in simulations matched the experiments reasonably well. The experimental force-displacement measurements of a representative dog-bone shaped sample (Sample #6) is given in [Fig. 5](#) where the crack initiated at 2.115 mm displacement and was fully propagated at 2.671 mm. During the experimental tissue rupture process, the crack initiated at the border of the soft inclusion, as shown in [Fig. 6](#), left panel.

According to the computational results depicted in [Fig.6](#), the higher amount of strain energy density was located around the soft inclusion at the sides in both Neo-Hookean and HGO material models combined with lower SED at the north and south parts of the inclusion, reflecting the crack initiation point. Despite the uniform high strain energy distribution spanning a large region in the central part in the Neo-Hookean model, the HGO_{aniso} model presented a smaller high SED region, localised at the edges of the inclusion. In [Fig.6](#) the computational results of Neo-Hookean and HGO_{aniso} models are illustrated due to the crack initiation similarity between HGO_{iso} and HGO_{aniso} models.

Comparing the “ideal” and “image-based” simulations, both Neo-Hookean models converged with similar outcome. As far as the crack propagation pattern is concerned, all models followed the experimental crack path but the “image-based” models presented a more similar crack propagation pattern with the experimental data as the soft inclusion ended up deformed and with thinner tissue in the middle section. The Neo-Hookean models resulted in uniform strain energy distribution affecting the entire tissue and not only the middle region while the opposite distribution was observed in HGO models.

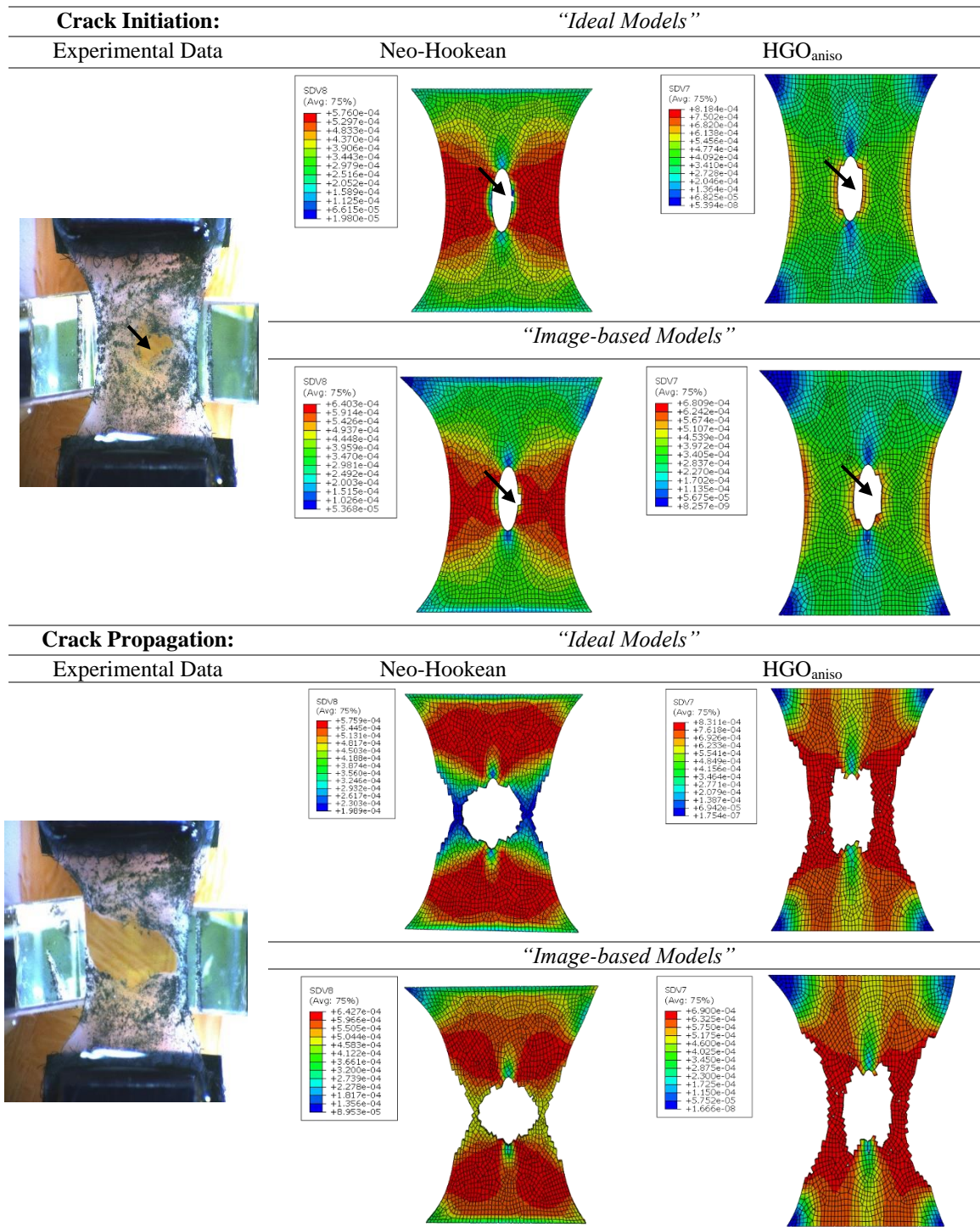


Fig.6. A representative example case of qualitative crack initiation and propagation comparison between experimental data and HGO with zero K value computational simulations following the SEDF with energy limiter damage model. The variables SDV7, 8 illustrated the SEDF in MPa.

Overall, 62% of the computational models (26 cases out of 42: all "ideal" and "real" Neo-Hookean models, 16 HGO "ideal" and 16 HGO "real" models) resulted in the same crack initiation point with the tissue-engineered samples ([Appendix D](#)). The remaining 16 cases (all HGO material models) showed no crack initiation under the prescribed boundary conditions and strain energy limiter thresholds. In addition, 20 out of 24 "ideal" models resulted in more than one crack initiation points around the inclusion, compared with the "image-based" models. With respect to the SED distribution map, the isotropic models, namely the Neo-Hookean and HGO_{iso}, showed a more uniform energy distribution with higher values in the middle section of the sample and especially around the inclusion.

However, in the HGO_{aniso}, the higher amount of energy was located only at the edges of the inclusion or the outer edges of the tissue and not in the whole middle section of the model, as shown in Fig. 6 of the representative example.

Due to the lack of crack initiation points in 16 cases, 26 computational models were compared with the experimental data regarding the crack propagation pattern. About 77% of these models (20 cases out of 26) successfully simulated the crack path with multiple cracks at the inclusion and tissue outer border (Appendix D). The crack propagation patterns presented in the “image-based” models resembled the corresponding experimental data better than the “ideal” models. Regarding the SED distribution, a uniform energy distribution around the soft inclusion is presented. The damage mechanism in Neo-Hookean models influenced the whole tissue sample resulted in a more uniform strain energy distribution while the HGO models presented the highest amount of energy in the thinnest parts of the models and specifically in the HGO_{aniso} the higher SED was spread across the fiber direction.

3.2 Quantitative assessment

The quantitative analysis of both material models (Neo-Hookean and HGO) focused on the first damaged element (the first element that reached the energy limiter) within the middle section of the computational models. Regarding the representative example (Sample #6), the HGO_{aniso} presented greater maximum principal Cauchy stress, while the Neo-Hookean and the HGO_{iso} resulted in similar mechanical behavior, as shown in Fig. 7. With reference to the geometrical categories: “ideal” and “image-based” models, in the HGO simulations the “ideal” case presented higher Cauchy stresses in contrast with the Neo-Hookean models. In addition, the experimental mechanical behavior is illustrated emphasizing on the sudden and sharp drop of the experimental curve compared to the computational results.

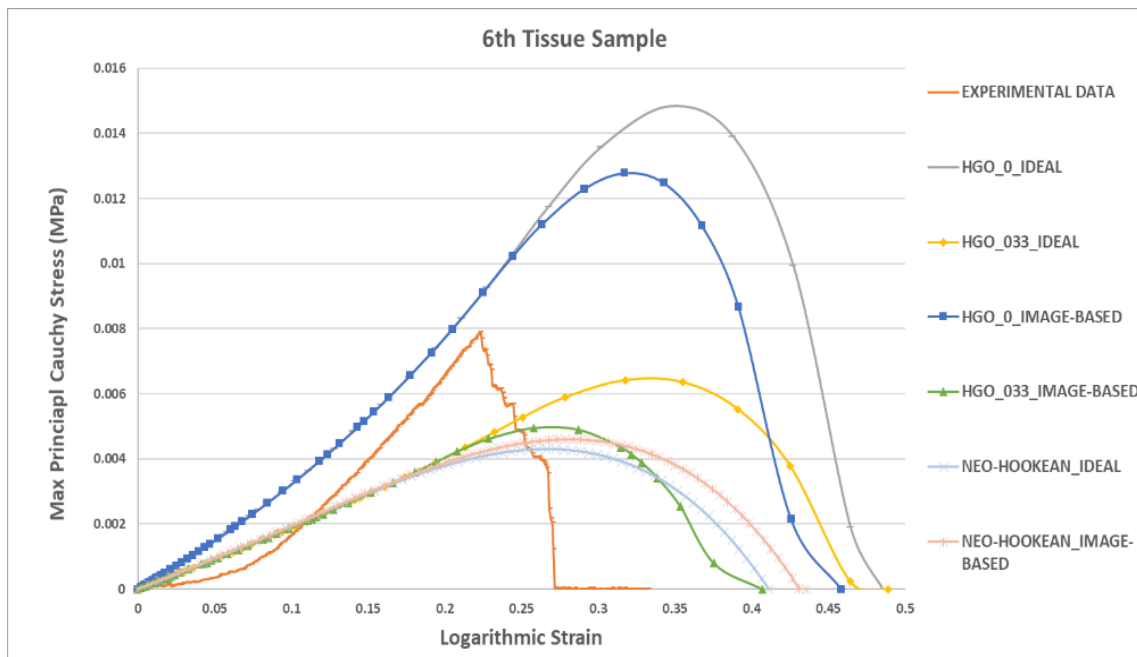


Fig. 7. Experimental and computational results of the tissue sample #6 regarding the Maximum Principal Cauchy Stress vs Logarithmic strain data.

According to Fig.8 presenting the SEDF with energy limiter of the first damaged element of the representative example (Sample #6), the HGO_{aniso} provided the highest maximum of strain energy, approximately 65% higher than the Neo-Hookean models. Even though, in the HGO material models the “ideal” cases introduced about 50% higher amount of strain energy compared with “imaged-based”

models, in the Neo-Hookean model the “image-based” simulations resulted in slightly higher amount of strain energy delaying 10% of total time the fully-damaged condition.

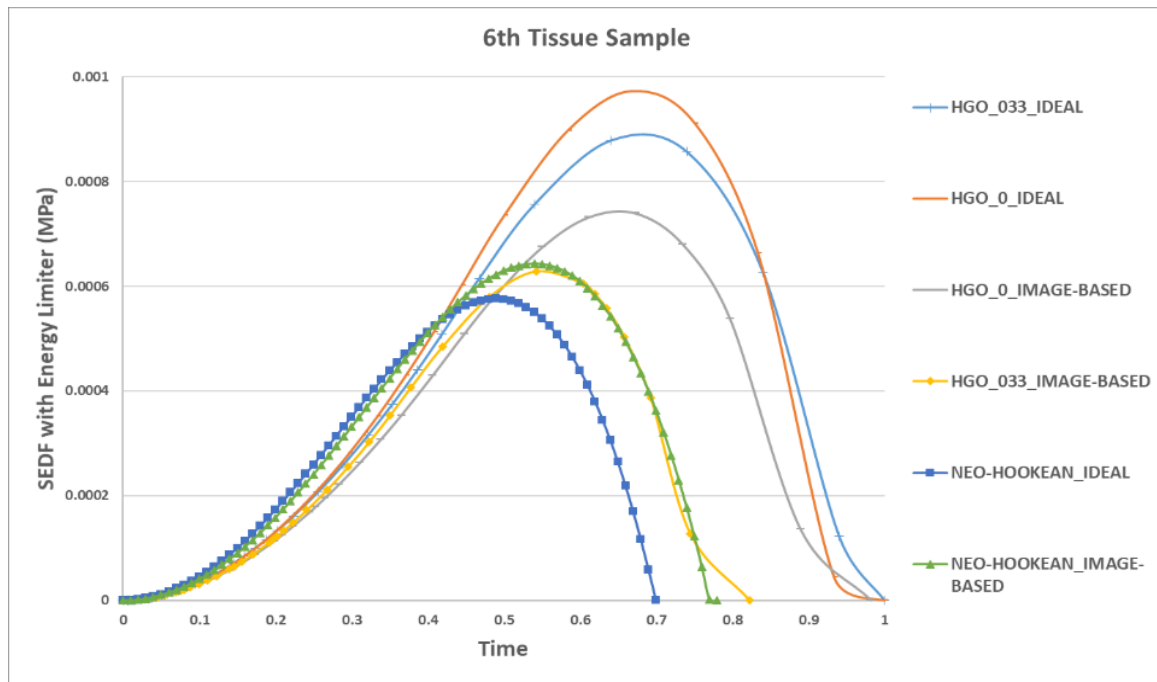


Fig. 8. Experimental and computational results of the tissue sample #6 regarding the SEDF with energy limiter vs simulation Time data.

In overall, with reference to the Cauchy stress-logarithmic strain graphs of the first damaged element within the middle section of all computational models ([Appendix E](#)), the higher maximum principal Cauchy stresses were generated with the HGO_{aniso} while the HGO_{iso} and the Neo-Hookean models resulted in similar stress distribution. Regarding the HGO_{aniso} , half of the “ideal” models presented significantly lower stresses compared to the “image-based” models illustrating the influence of the accurate geometric representation.

The experimental Cauchy stress-logarithmic strain results showed a sharp decrease in stress in the “damaged region” compared with a “smoother” and slower damage model of the computational models. The total separation of the experimental tissue occurred roughly at half of the logarithmic strain value of the first damaged element in computational models (both Neo-Hookean and HGO).

A quantitative comparison between the Neo-Hookean and HGO material models demonstrated that in all 8 cases the HGO_{aniso} model had a higher amount of SED reflecting the importance of the anisotropy due to the fiber alignment ([Appendix E](#)). The geometrical irregularities in the samples slightly affected the amount of energy in each model as 80% (19 out of 24 cases) of “ideal” and “image-based” models converged with equivalent results.

Comparing the Neo-Hookean and HGO models it was clear that the Neo-Hookean model presented a more “linear” and rapid damage, which reached the completely developed damage at approximately 70% of total analysis time. Although the HGO_{iso} model and the Neo-Hookean model presented an isotropic behavior, the former resulted in higher amount of energy because the HGO_{iso} model focuses on the isotropic contribution as the fibers are still incorporated inside the tissue but randomly distributed.

3.3 Parametric Study Results

The results of the parametric analysis of multiple energy limiters in matrix and fibres components are summarised in Fig. 9 with 8 different curves. All 8 curves were smooth with gradual material degradation. It was clear from the analysis that the higher the matrix crack initiation threshold, the higher the amount of energy that could be stored in the tissue. The amount of energy stored by fibres component was significantly reduced and the fibres part was not able to carry extra loads or store additional energy and consequently the main component that affected the model's damage behaviour was the matrix part.

The models with lowest amount of strain energy that reached the fully damaged state at 0.5 total time and the models with maximum amount of stored energy in the tissue were the simulations with matrix crack initiation threshold set at 20% (minimum) and 80% (maximum), respectively, regardless of the fibrous part crack thresholds. As a result, the damage model could be characterised as matrix-dominated due to the diminished influence of fibrous part in the SEDF with energy limiter damage model.

Specifically, in 2 cases where the matrix crack initiation started at 0.4 and 0.6 total time and the fibrous part initially cracked at 0.6 and 0.8 total time, the final fully damaged state delayed approximately 10% of total time. In the computational models with matrix crack initiation threshold set at 60% and 80% of total time combined with fibrous part crack initiation at 20% of the total time, the amount of stored energy in the tissue was reduced about 3-4%.

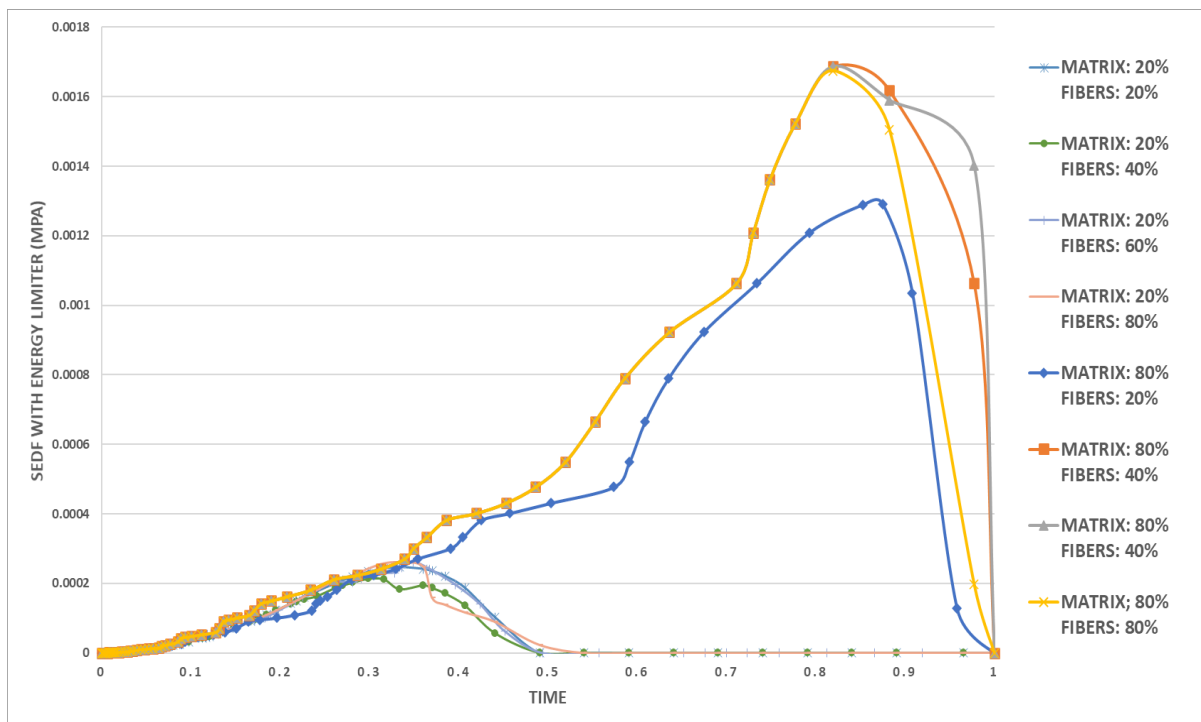


Fig. 9. 8 curves of tissue SEDF with energy limiter vs simulation time regarding all crack initiation threshold combinations between matrix and fibrous components at 20%, 40%, 60% and 80% of total time.

4. Discussion

In the present study the SEDF with energy limiter damage model was developed. This damage modeling approach has already been used for various applications, including soft biological tissue damage modelling ([Simo, 1985](#); [Calvo et al., 2006](#); [Rodriguez et al., 2008](#); [Volokh, 2011](#)) but to the best of the authors' knowledge, this is the first time that this approach is used for plaque rupture analysis. The damage model was first implemented in two hyper-elastic material models (Neo-Hookean and HGO) via material user subroutines (UMAT codes) in ABAQUS and then the models were used to capture the damage in uniaxial tensile plaque-mimicking tissue-engineered experiments. The generated computational models with idealized and realistic geometrical configurations focused on studying the crack initiation and propagation patterns identifying the peak and the distribution of SED.

During the identification and evaluation of the material parameters for both Neo-Hookean and HGO material models a least-square optimization algorithm was implemented based on the first 20 nominal stress-strain values of the initial experimental tissue sample. The results suggested that the Neo-Hookean model fitted reasonably well the experimental data, which, compared to HGO models, demonstrated higher Strain Energy Density values. The results were in accordance with the literature, as in the article of [Merei et al.](#), regarding the atherosclerotic plaque delamination process, the Neo-Hookean material parameters were identified with an inverse method. In addition, the Neo-Hookean model was compared with the HGO model from the [Leng et al.](#) study and the Neo-Hookean model matched adequately the experimental data with less fitting issues due to the reasonably reduced values of elastic strains at the beginning of the delamination process ([Leng et al., 2015](#); [Merei et al., 2017](#)).

The damage initiation location was found to be sensitive to the geometrical configuration as the “ideal” computational models resulted in more than one crack initiation points compared to the “image-based” models due to the idealized and symmetrical configuration. In addition, high deviation (maximum of 65%) between “ideal” and “real” models regarding the Cauchy stress and strain energy density values was observed. Another geometrical formation that controlled the crack initiation mechanism was the central soft inclusion. Irrespective of the configuration, the damage initiated from the inclusion and propagated horizontally towards the outer edges in the middle region. In the study of [Saez et al.](#) a damage model for soft fibrous tissues was described regarding the SEDF in the hyper-elastic framework and a microsphere approach. The damage initiation in the microsphere-based simulations was around the tissue-sphere interface due to the high level of stress and energy concentration ([Saez et al., 2012](#)).

According to the results of the quantitative analysis, the HGO_{aniso} presented the highest amount of maximum principal Cauchy stresses and strain energy in all simulations due to the incorporated fiber-family of the HGO models. Especially when the fibers were fully aligned in the loading direction (HGO_{aniso}) as they could bear greater load and store greater energy within the tissue. Comparing the results of HGO_{iso} and the Neo-Hookean models, both resulted in similar Cauchy stress distribution reflecting their isotropic contribution but the HGO_{iso} model could store higher amount of strain energy as the fiber-family was still integrated but randomly distributed ([Holzapfel et al., 2014](#)).

It is remarkable that 16 HGO computational models demonstrated no crack initiation points. Factors that may contribute to that divergent results include the simplifications, approximations and uncertainties in the models that influenced the local mechanical response, such as the complex geometry, the evaluation of the material properties and the heterogeneity of a soft biological tissue. In the study of [Pena et al.](#), the constitutive parameters of phenomenological and microstructural damage models, within continuum damage mechanics framework, were calculated highlighting the effect of the heterogeneity in arteries with layer-specific damage models and the implementation of different damage parameters in axial and circumferential directions ([Weisbecker et al., 2012](#); [Pena et al., 2019](#)).

In the parametric study of SEDF with various energy limiters the matrix and fibers components were decoupled and the crack initiation thresholds were calculated as a percentage of total analysis time. With reference to the results, the matrix contribution significantly influenced the damage model as it presented higher amount of energy stored and the fibers part delayed the fully damaged state 10% of time in only 2 cases. The results are in accordance with the data reported by Oliviera et al. where the SEDF with energy limiter damage model was implemented for pelvic muscle applications separating the damage parameters between extracellular matrix and muscle fibers resulting in matrix-controlled damage model. Specifically, during the damage evolution, the matrix part damage growth was higher than the fibers damage contribution ending up with 60% variation in their damage values ([Oliviera et al., 2016](#)). However, in muscle injuries the fiber families were fully damaged and the matrix component remained intact until the next trauma ([Baratz et al. 1999](#)).

Although the computational damage models provided reasonable results compared with experimental data, several simplifications and approximations during the material evaluation process were implemented. In the HGO material model one fiber family was assumed and the fibers were either fully aligned in the loading direction or randomly distributed due to the lack of experimental structural data. Even in the least-square optimization algorithm, few restrictions were implemented such as the tolerance and the number of iterations with non-negative results in order to minimize the solution field. Consequently, a unique solution could not be guaranteed. Furthermore, the material evaluation and mesh convergence analysis were conducted in the initial experimental case but implemented in all computational models assuming that the same experimental protocol was followed in all experimental cases.

A future improvement of this study would include the implementation of the SEDF with energy limiter damage model in the elasticity tensor of the HGO material model in order to provide rapid and accurate results through finite element software via a fully automated process. The damage model could be also further validated using more realistic experimental and in-silico models in an attempt to understand better the plaque rupture mechanism. As a long-term goal, clinical applications of the damage model could also be a future investigation regarding patient-specific atherosclerotic plaque ruptured samples implementing the mechanical properties of human plaque tissue presented in the article of Akyildiz et al. in order to predict the atherosclerotic plaque rupture risk in patients ([Akyildiz et al., 2014](#)).

5. Conclusion

A comprehensive approach of Strain Energy Density Function with energy limiter damage model is described in the present study for studying atherosclerotic plaque rupture. The damage model was numerically developed and implemented in a commercial finite element software and its use was demonstrated for atherosclerotic plaque-mimicking tissue-engineered samples. The energy thresholds were implemented in the SEDF of Neo-Hookean and Holzapfel-Gasser-Ogden models due to the hyper-elasticity of soft biological tissues, like atherosclerotic plaque, via material user subroutines. In the material evaluation process an iterative optimization algorithm was generated. Overall, the damage predictions regarding the crack initiation and propagation patterns in computational models fitted reasonably well the experimental results reflecting a geometrical configuration sensitivity. The anisotropic HGO model presented the highest amount of stored energy and in case of multiple energy limiters applied the damage model could be characterized as matrix dominated. Refining the numerical damage model will enable possibly an optimum agreement with experimental data leading to a better understanding of plaque rupture mechanism.

References

- ABAQUS, 2016. Analysis user's manual version 6.14, Dassault Systemes Corp.
- Akyildiz, A.C., Speelman, L., Gijsen, F., 2014. Mechanical properties of human atherosclerotic intima tissue. *J. Biomech.* 47.
- Akyildiz, A.C., Hansen, H.H., Nieuwstadt, H.A., 2016. A Framework for Local Mechanical Characterization of Atherosclerotic Plaques: Combination of Ultrasound Displacement Imaging and Inverse Finite Element Analysis. *Ann. Biomed. Eng.* 44(4),968-979.
- Akyildiz, A.C., Speelman, L., van Velzen, B., Stevens, R.R.F., van der Steen, A.F.W., Huberts, W., Gijsen, F., 2018. Intima heterogeneity in stress assessment of atherosclerotic plaques. *Interface Focus.* 8, 20170008.
- Badel, P., Avril, S., Lessner, S.M., Sutton, M.A., 2011. Mechanical identification of layer-specific properties of mouse carotid arteries using 3D-DIC and a hyperelastic anisotropic constitutive model. *Comput. Methods Biomech. Biomed. Eng.* 15(1), 37-48.
- Badel, P., Avril, S., Sutton, M.A., Lessner, S.M., 2014. Numerical simulation of arterial dissection during balloon angioplasty of atherosclerotic coronary arteries. *J. Biomech.* 47, 878–889.
- Baratz, M.E., Watson, A.D., Imbriglia, J.E. & Fowler, J.E. 1999. *Orthopaedic Surgery: The Essentials* 1st Edition. New York, NY: Thieme.
- Calvo, B., Peña, E., Martinez, M.A. and Doblaré, M., 2007. An uncoupled directional damage model for fibred biological soft tissues. Formulation and computational aspects. *Int. J. Numer. Meth. Eng.*, 69, 2036-2057.
- deBotton, G., Hariton, I., Socolsky, E.A., 2006. Neo-Hookean fiber-reinforced composites in finite elasticity. *J. Mech. Phys. of Solids.* 54(3), 533-559.
- Famaey, N., Sloten, J.V., Kuhl, E., 2013. A three-constituent damage model for arterial clamping in computer-assisted surgery. *Biomech. Model Mechanobiol.* 12, 123–136.
- Fehervary, H., Maes, L., Vastmans, J., Kloosterman, G., Famaey, N., 2020. How to implement user-defined fiber-reinforced hyperelastic materials in finite element software. *J. Mech. Behav. Biomed. Mater.* 110, 103737.
- Ferrara, A., Pandolfi, A., 2008. Numerical modelling of fracture in human arteries. *Comput. Methods Biomech. Biomed. Eng.* 11(5), 553-567.
- Ferreira, J.P.S., Parente, M.P.L., Jabareen, M., 2017. A general framework for the numerical implementation of anisotropic hyperelastic material models including non-local damage. *Biomech Model Mechanobiol.* 16, 1119–1140.
- Gasser, T.C., Holzapfel, G.A., 2006. Modeling the propagation of arterial dissection. *Europ. J. Mech. a-Solids.* 25(4), 617-633.
- Gasser, T.C., Holzapfel, G.A., 2007. Modeling Plaque Fissuring and Dissection during Balloon Angioplasty Intervention. *Ann. Biomed. Eng.* 35(5), 711–723.
- Gultekin, O., Dal, H., Holzapfel, G.A., 2016. A phase-field approach to model fracture of arterial walls: Theory and finite element analysis. *Comput. Methods Appl Mech Eng.* 312, 542-566.
- Hajhashemkhani, M., Hematiyan, M., 2015. Determination of material parameters of isotropic and anisotropic hyper-elastic materials using boundary measured data. *J. Theor. Appl. Mech.* 53, 895-910.
- Holzapfel, G.A., Mulvihill, J.J., Cunnane, E.M., Walsh, M.T., 2014. Computational approaches for analyzing the mechanics of atherosclerotic plaques: A review. *J. Biomech.* 47(4), 859-869.
- Huang, Y., Teng, Z., Sadat, U., 2013. In vivo MRI-based simulation of fatigue process: a possible trigger for human carotid atherosclerotic plaque rupture. *BioMed Eng OnLine.* 12, 36.
- Leng, X., Chen, X., Davis, L., Deng, X., Sutton, M.A., Lessner, S.M., 2015. Modeling of Experimental Atherosclerotic Plaque Delamination. *Ann. Biomed. Eng.* 43(12), 2838–2851.

- Leng, X., Davis, L., Deng, X., Sutton, M.A., Lessner, S.M., 2016. Numerical modeling of experimental human fibrous cap delamination. *J. Mech. Behav. Biomed. Mater.* 59, 322–336.
- Merei, B., Badel, P., Davis, L., Avril, S., Sutton, M.A., Lessner, S.M., 2017. Atherosclerotic Plaque Adhesion Strength and its role in Plaque Rupture. *J. Mech. Behav. Biomed. Mater.* 67, 19–30
- Mousavi, S.J., Farzaneh, S., Avril, S., 2018. Computational predictions of damage propagation preceding dissection of ascending thoracic aortic aneurysms. *Inter. J. Numerical Methods in Biomed. Eng.* 34(4).
- Nolan, D., Lally, C., & McGarry, P., 2019. Understanding the deformation gradient in Abaqus and key guidelines for anisotropic hyperelastic user material subroutines (UMATs). *engrXiv*.
- Oliveira, D., Parente, M.P., Natal Jorge, R.M. (Eds), 2016. The biomechanical effect of damage on the pelvic floor muscles behavior. *BioMedWomen*. pp. 193-196.
- Pahwa, R., Goyal, R., Bansal, P., Jialal, I., 2020. *Chronic Inflammation*. StatPearls Publishing.
- Pei, X., Wu, B., Li, Z., 2013. Fatigue crack propagation analysis of plaque rupture. *J Biomech. Eng.* 135(10), 101003-101009.
- Peña, E., Calvo, B., Martínez, M.A. & Doblare, M. 2008. On finite-strain damage of viscoelastic fibred materials. Application to soft biological tissues. *Int J. Numer Methods Eng.* 74(7), 1198–1218.
- Peña, E., 2011. Damage functions of the internal variables for soft biological fibred tissues. *Mech. Res Commun.* 38(8), 610-615.
- Peña, J.A., Martínez, M.A., Peña, E., 2019. Failure damage mechanical properties of thoracic and abdominal porcine aorta layers and related constitutive modeling: phenomenological and microstructural approach. *Biomech. Model Mechanobiol.* 18(6), 1709-1730.
- Rodriguez, J.F., Alastrue, V., Doblare, M., 2008. Finite element implementation of a stochastic three-dimensional finite-strain damage model for fibrous soft tissue. *Comput. Methods Appl. Mech. Eng.* 197(9–12), 946-958.
- Saez, P., Alastrue, V., Peña, E., Doblare, M., Martínez, M.A., 2012. Anisotropic microsphere-based approach to damage in soft fibered tissue. *Biomech. Model Mechanobiol.* 11(5), 595-608.
- Serra, S., 2020. *Mechanical Characterization of Tissue Engineered Fibrous Cap Constructs*. Master Thesis, BioMedical Engineering Department, Delft University of Technology.
- Simo, J.C., 1985. On a fully three-dimensional finite-strain viscoelastic damage model: Formulation and computational aspects. *Comput. Methods Appl. Mech. Eng.* 60(2), 153-173.
- Sun, W., Chaikof, E.L., Levenston, M.E., 2008. Numerical Approximation of Tangent Moduli for Finite Element Implementations of Nonlinear Hyperelastic Material Models. *ASME. J Biomech Eng.* 130(6), 061003.
- Versluis, A., Bank, A.J., Douglas, W.H., 2006. Fatigue and plaque rupture in myocardial infarction. *J Biomech. Eng.* 39(2), 339-347.
- Virmani, R., Burke, A.P., Kolodgie, F.D., Farb, A., 2002. Vulnerable plaque: the pathology of unstable coronary lesions. *J. Interv. Cardiol.* 15(6), 439–446.
- Virmani, R., Narula, J., Leon, M.B., Willerson, J.T. (Eds.), 2007. *The Vulnerable Atherosclerotic Plaque: Strategies for Diagnosis and Management*. Blackwell Futura, Malden, MA, pp. 37–59.
- Volokh, K.Y., 2011. Modelling failure of soft anisotropic materials with application to arteries. *J. Mech. Behav. Biomed. Mater.* 4(8), 1582-1594.
- Weisbecker, H., Pierce, D.M., Regitnig, P., Holzapfel, G.A., 2012. Layer-specific damage experiments and modeling of human thoracic and abdominal aortas with non-atherosclerotic intimal thickening. *J. Mech. Behav. Biomed. Mater.* 12, 93-106.

Appendix A.1

The implementation of the SEDF with energy limiter damage model in finite element software comprised the development of the Neo-Hookean and HGO material models via material user subroutines written in Fortran. The numerical development of material user subroutine (UMAT code) in ABAQUS 2016 of both hyper-elastic material models (Neo-Hookean and HGO) included the constitutive equations of Cauchy Stress and Elasticity Tensor, as presented in [Table 3](#).

Table 3. The numerical calculations of Cauchy stress and Elasticity tensor of Neo Hooken and HGO material models ([Fehervary et al., 2020](#); [Nolan et al., 2020](#)).

Neo-Hookean Material Model	Cauchy Stress (σ):	$\sigma = \frac{2}{J} C_{10} (B - \frac{1}{3} \text{trace}(B) \cdot I) + \frac{2}{D_1} (J-1) \cdot I$
	Elasticity Tensor (h):	$h_{ijkl} = \frac{2}{J} C_{10} (\frac{1}{2} \delta_{ij} B_{kl} - \frac{2}{3} \delta_{kl} B_{ij}) + \frac{2}{D_1} (2J-1) \cdot \delta_{ij} \delta_{kl}$ where $\delta_{ij} = F_{ik} \cdot F_{kj}^{-1}$ is the Kronecker delta.
HGO Material Model	Cauchy Stress (σ):	$\sigma = \frac{2}{J} C_{10} (B - \frac{1}{3} \delta_{ij} \cdot I_1) + \frac{2k_1}{J} \exp(k_2 E^2) \cdot E [k \cdot (B - \frac{1}{3} \delta_{ij} \cdot I_1) + (1-3k) \cdot (m_i \cdot m_j - \frac{1}{3} \delta_{ij} \cdot I_4) + \frac{1}{D_1} (J - \frac{1}{J}) \cdot \delta_{ij},$ $E = \kappa (I_1 - 3) + (1 - 3\kappa) \cdot (I_4 - 3)$
	Elasticity Tensor (h):	$h_{ijkl} = \frac{2}{J} C_{10} \cdot [-\frac{2}{3} \delta_{kl} B_{ij} + \frac{2}{9} \delta_{ij} \delta_{kl} I_1 + \frac{1}{2} (\delta_{il} B_{kj} + \delta_{ik} B_{jl} + \delta_{jk} B_{il}) - \frac{1}{3} (\delta_{ij} B_{lk} + \delta_{ij} B_{kl})] + \frac{2k_1}{J} \exp(k_2 E^2) \cdot [E \cdot k \cdot (\delta_{kl} B_{ij} - \frac{1}{3} \delta_{ij} \delta_{kl} I_1) + E \cdot (1-3k) \cdot (m_i \cdot m_j \delta_{kl} - \frac{1}{3} \delta_{ij} \delta_{kl} I_4) + [-\frac{5}{3} E \cdot k \cdot \delta_{kl} + (2k_2 \cdot E^2 + 1) \cdot k^2 \cdot (B_{kl} + B_{lk} - \frac{2}{3} \delta_{kl} I_1)] \cdot (B_{ij} - \frac{1}{3} \delta_{ij} I_1) + E \cdot k \cdot [\frac{1}{2} \cdot (\delta_{ik} B_{lj} + \delta_{jk} B_{il} + \delta_{il} B_{kj} + \delta_{jl} B_{ik}) - \frac{1}{3} (B_{kl} \delta_{ij} + B_{lk} \delta_{ij}) + [-\frac{5}{3} E \cdot (1-3k) \delta_{kl} + (2k_2 \cdot E^2 + 1) \cdot (1-3k)^2 \cdot (2 m_k \cdot m_l - \frac{2}{3} \delta_{kl} I_4)] \cdot (m_i \cdot m_j - \frac{1}{3} \delta_{ij} I_4) + E \cdot (1-3k) \cdot [\frac{1}{2} \cdot (m_i \cdot m_j \delta_{ik} + m_i \cdot m_l \delta_{jk} + m_k \cdot m_j \delta_{il} + m_i \cdot m_k \delta_{jl}) - \frac{2}{3} m_l \cdot m_k \delta_{ij}] + \frac{2}{D_1 J} \delta_{ij} \delta_{kl}]$

The tangent matrix of HGO material model, presented in [Table 3](#), could be also estimated using a “numerical approximation” method with small perturbations ($1 \cdot e^{-8}$) in all directions of the deformation gradient. The method is based on the estimated Kirchhoff stresses and not on any material model as the exact tangent moduli are not necessary to achieve precise solutions ([Sun et al., 2008](#); [Fehervary et al., 2020](#); [Nolan et al., 2020](#)).

The Holzapfel- Gasser- Ogden UMAT

```

DIMENSION SKIRCH(3,3), STRS(3,3), MAT(3,2), I4(2), R(3,3),
1          U(3,3), RT(3,3), XAM(3,1), XAM1(3,1)
C-----
NANISO = 1
C-----
PI = 3.14159265359
THETAT1 = THETA1*PI/180.0
THETAT2 = THETA2*PI/180.0
C
MAT(1,1)=COS(THETAT1); MAT(2,1)= SIN(THETAT1); MAT(3,1)=0.
MAT(1,2)=COS(THETAT2); MAT(2,2)= SIN(THETAT2); MAT(3,2)=0.
C-----
CALL kpolarDecomp(DFGRD1, U, R)
RT = transpose(R)
C-----
DO IAN = 1,NANISO
  XAM(:,1) = MAT(:,IAN)
C
  XAM1 = MATMUL(RT,XAM)
C
  MAT(:,IAN) = XAM1(:,1)

```

```

END DO
C-----
CALL KirStress(DFGRD1, C10, D1, kap, k1, k2, SKIRCH, J,
1      MAT, I1, I2, I4, NPT, NANISO, iter, WE)
C-----
STRS = SKIRCH / J
C
CALL kmatrix2vector(STRSS, STRESS, nshr)
C-----
CALL kCTM(SKIRCH,DFGRD1,NTENS,PROPS,MAT,NPT,ITER,
+      NANISO, DDSDE, NPROPS, J, NSHR)
C
RETURN
C
END SUBROUTINE UMAT
C-----
C      SUBROUTINES
C-----
SUBROUTINE KirStress (DGRAD, C10, D1, kap, k1, k2, SKIRCH,
1      J, MAT, I1, I2, I4, NPT, NANISO, iter, WE)
C
INCLUDE 'ABA_PARAM.INC'
C
INTENT(IN) :: DGRAD, C10, D1, kap, k1, k2, MAT, NANISO, iter
INTENT(OUT):: SKIRCH, J, I1, I2, I4, WE
C
DIMENSION DGRAD(3,3), BMAT(3,3), SKIRCH(3,3), MAT(3,2),
1      XA(3), FIBER(3), MAFIBER(3,3), ANISOK(3,3),
2      ANISOTOT(3,3), I4(2)
C
J = DGRAD(1, 1)*DGRAD(2, 2)*DGRAD(3, 3)
1  -DGRAD(1, 2)*DGRAD(2, 1)*DGRAD(3, 3)
2  +DGRAD(1, 2)*DGRAD(2, 3)*DGRAD(3, 1)
3  +DGRAD(1, 3)*DGRAD(3, 2)*DGRAD(2, 1)
4  -DGRAD(1, 3)*DGRAD(3, 1)*DGRAD(2, 2)
5  -DGRAD(2, 3)*DGRAD(3, 2)*DGRAD(1, 1)
C
BMAT = MATMUL(DGRAD,TRANSPOSE(DGRAD))
C-----
I1 = BMAT(1,1) + BMAT(2,2) + BMAT(3,3)
C-----
DO IANISO = 1,NANISO
  XA = MAT(1:3,IANISO);
  FIBER = MATMUL(DGRAD,XA)
C
  DO i=1,3
    DO j=1,3
      MAFIBER (i,j) = FIBER (i) * FIBER (j)
    ENDDO
  ENDDO
C
  I4(IANISO) = MAFIBER (1,1) + MAFIBER (2,2) + MAFIBER (3,3)
  EA = kap*(I1 - 3.D0) + (1.D0 - 3.D0*kap)*(I4(IANISO)-1.D0)
  EAA = k2*(EA)**2
C
  WE = C10*(I1 - 3.D0)
1  + (1.D0/D1)*((J**TWO - 1.D0)/2.D0 - LOG(J))
2  + (k1/2.D0*k2)*((exp(EAA) - 1.D0)
C
  PART1 = TWO*(C10 + exp(EAA)*kap*EA*k1)/(J**(TWO/THREE))
  TRBMAT= PART1*(BMAT(1,1)+BMAT(2,2)+BMAT(3,3))/THREE
  SKIRCH = PART1 * BMAT
C
  DO I = 1,3
    SKIRCH(I,I) = SKIRCH(I,I) - TRBMAT
  END DO
C
  PART2 = 2*(J-ONE)*J/D1
C
  DO I = 1,3

```

```

        SKIRCH(I,I) = SKIRCH(I,I) + PART2
    END DO
C
    term1 = 2.0*k1;
    term2 = EA*(1.D0 - 3.D0*kap)
    term4 = exp(EAA)
    ANISOK = term1*term2*term4*MAFIBER
    ANISOTOT = ANISOTOT + ANISOK
C
END DO
C
SKIRCH = SKIRCH + ANISOTOT
C
RETURN
END SUBROUTINE KirStress
C
SUBROUTINE kCTM(SKIRCH1,DFGRD1,NTENS,PROPS,MAT,NPT,ITER,
+
                NANISO, DDSDE, NPROPS, J1, NSHR)
C
DIMENSION SKIRCH1(3,3), DFP(3,3), DFGRD_PERT(3,3),SKIRCH_PERT(3,3)
1 ,          CMJ(3,3), CMJVEC(NTENS), ilist(6), jlist(6), MAT(3,2), I4(2)
2 ,          DFGRD1(3,3), DDSDE(NTENS,NTENS), PROPS(NPROPS)
C
C Perturbation parameter
eps = 1.0e-08
C
i1ist(1) = 1; j1ist(1) = 1;
i1ist(2) = 2; j1ist(2) = 2;
i1ist(3) = 3; j1ist(3) = 3;
i1ist(4) = 1; j1ist(4) = 2;
i1ist(5) = 1; j1ist(5) = 3;
i1ist(6) = 2; j1ist(6) = 3;
C
Perturbation: DO iter = 1,NTENS
C-----
    ii = i1ist(iter)
    jj = j1ist(iter)
    CALL kdelF(ii, jj, DFGRD1, eps, DFP)
    DFGRD_PERT = DFGRD1 + DFP
C-----
    CALL KirStress (DFGRD_PERT, C10, D1, kap, k1, k2,
1 SKIRCH_PERT, JP, MAT, I1, I2, I4, NPT, NANISO,
2 iter, WE)
C-----
    CMJ = SKIRCH_PERT - KIRCH1
    CMJ = CMJ/J1/eps
    CALL kmatrix2vector(CMJ, CMJVEC, NSHR)
    DO insert = 1,NTENS
        DDSDE(insert,iter) = CMJVEC(insert)
    END DO
END DO Perturbation
END SUBROUTINE kCTM
C-----
SUBROUTINE kmatrix2vector(XMAT, VEC, NSHR)
INCLUDE 'ABA_PARAM.INC'
intent(in) :: XMAT, NSHR
intent(out):: VEC
dimension xmat(3,3), vec(6)
DO i=1,3
    vec(i) = xmat(i,i);
END DO
vec(4) = xmat(1,2);
IF (NSHR==3) then
    vec(5) = xmat(1,3);
    vec(6) = xmat(2,3);
END IF
END SUBROUTINE kmatrix2vector
END SUBROUTINE KMTMS
C-----
SUBROUTINE kdelF(m, n, DGRAD, eps, DF)

```

```

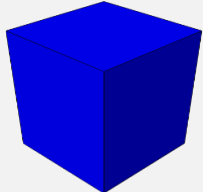
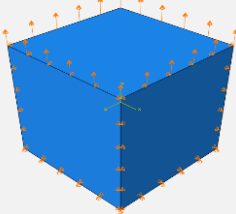
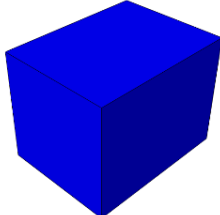
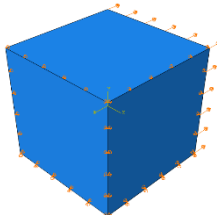
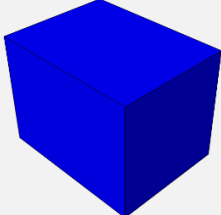
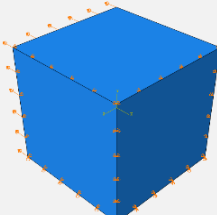
INCLUDE 'ABA_PARAM.INC'
intent (in) :: DGRAD, eps, m, n
intent (out):: DF
C   increment (eps)
dimension dyad1(3,3), dyad2(3,3), DGRAD(3,3), DF(3,3), DFp1(3,3)
C
DO i = 1,3
DO j = 1,3
dyad1(i,j) = zero
dyad2(i,j) = zero
END DO
END DO
dyad1(m,n) = 1.0;
dyad2(n,m) = 1.0;
C
CALL KMTMS(3, 3, 3, dyad1, 3, DGRAD, 3, DFp1, 3)
DF = DFp1
CALL KMTMS(3, 3, 3, dyad2, 3, DGRAD, 3, DFp1, 3)
DF = DF + DFp1
DF = 0.5*DF*eps
END SUBROUTINE kdelF

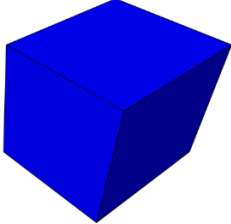
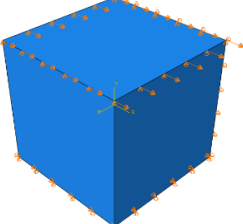
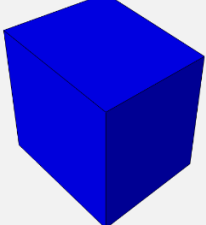
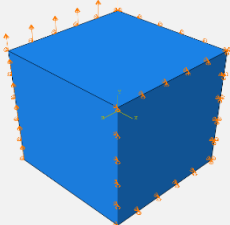
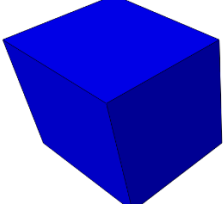
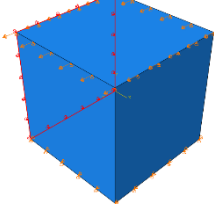
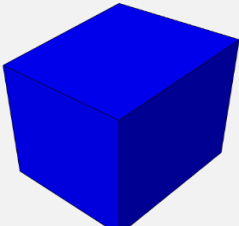
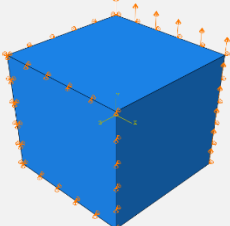
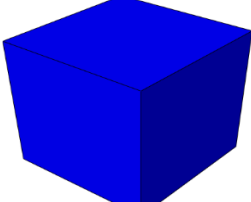
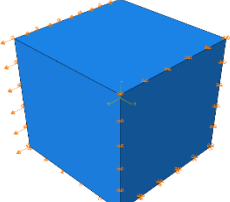
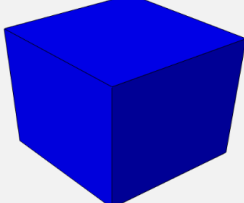
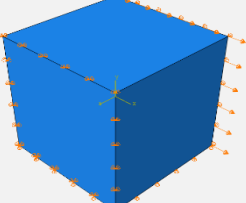
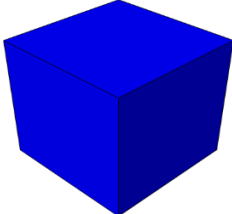
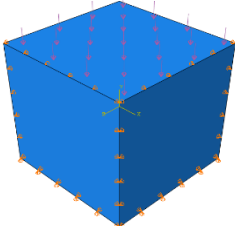
```

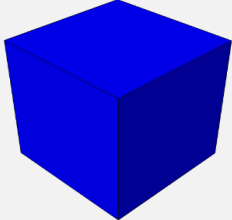
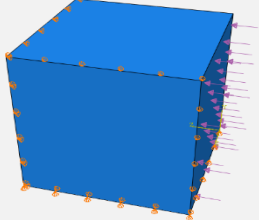
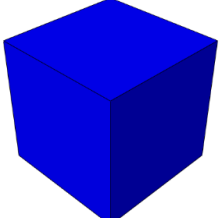
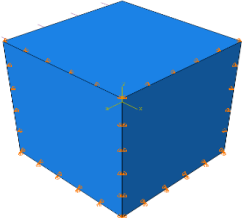
Appendix A.2

The Neo-Hookean UMAT code is provided by the ABAQUS Documentation 6.6 with the code verification files. During the verification process of HGO UMAT a solid incompressible, full integration, hybrid, hexahedral element was simulated (C3D8H) in the shape of cube with edges 50mm mimicking the verification process presented in the article of Fehervary et al. Furthermore, 12 loading cases were simulated in all directions X, Y, Z (3 stretch, 6 shear and 3 compression) with applied displacement of 10mm as presented in the [Table 4](#).

Table 4. The verification procedure of HGO UMAT code regarding 12 different loading conditions in all directions.

State	Sketch	Boundary Conditions
Stretch Y		 <p>The cube was fixed in y-direction in the XZ surface, fixed in z-direction in the XY surface and fixed in x-direction in the YZ surface. The displacement (10mm) was applied in y-direction.</p>
Stretch Z		 <p>The cube was fixed in y-direction in the XZ surface, fixed in z-direction in the XY surface and fixed in x-direction in the YZ surface. The displacement (10mm) was applied in z-direction</p>
Stretch X		 <p>The cube was fixed in y-direction in the XZ surface, fixed in z-direction in the XY surface and fixed in x-direction in the YZ surface. The displacement (10mm) was applied in x-direction</p>

Shear XY		 <p>The cube was fixed in y-direction in the upper XZ surface, fixed in z-direction in the XY surface and fixed in x- and y-direction in the lower XZ surface. The displacement (10mm) was applied in xy-direction</p>
Shear YX		 <p>The cube was fixed in x-direction in the upper YZ surface, fixed in z-direction in the XY surface and fixed in x- and y-direction in the lower YZ surface. The displacement (10mm) was applied in yx-direction</p>
Shear YZ		 <p>The cube was fixed in x-direction in the upper YZ surface, fixed in y-direction in the XZ surface and fixed in z- and y-direction in the lower XZ surface. The displacement (10mm) was applied in yz-direction</p>
Shear ZY		 <p>The cube was fixed in z-direction in the upper YX surface, fixed in x-direction in the YZ surface and fixed in z- and y-direction in the lower XY surface. The displacement (10mm) was applied in zy-direction</p>
Shear XZ		 <p>The cube was fixed in x-direction in the upper YZ surface, fixed in y-direction in the XZ surface and fixed in z- and x-direction in the lower ZY surface. The displacement (10mm) was applied in xz-direction</p>
Shear ZX		 <p>The cube was fixed in z-direction in the upper YX surface, fixed in y-direction in the XZ surface and fixed in z- and x-direction in the lower XY surface. The displacement (10mm) was applied in zx-direction</p>
Compression Y		 <p>The cube was fixed in y-direction in the XZ surface, fixed in z-direction in the XY surface and fixed in x-direction in the YZ surface. The force (0.04 N/mm) was applied in y-direction</p>

Compression Z			The cube was fixed in y-direction in the XZ surface, fixed in z-direction in the XY surface and fixed in x-direction in the YZ surface. The force (0.04 N/mm) was applied in z-direction
Compression X			The cube was fixed in y-direction in the XZ surface, fixed in z-direction in the XY surface and fixed in x-direction in the YZ surface. The force (0.04 N/mm) was applied in x-direction

According to the results of the verification process between already-implemented and UMAT HGO models, the Cauchy Stresses (S11, S22, S33, S12, S13, S23), the Reaction Forces (RF1, RF2, RF3) and the Displacements (U1, U2, U3) were the same in all stretch and compression models. Regarding the shear simulations, all models converged with no deviation results apart from two cases (Shear XZ and YZ) where the Cauchy Stresses and the Reaction Forces resulted in maximum relative error of 0.18% and 0.066% respectively. Besides the verification of single-element models, the multiple-elements model “adventitia_axial.inp” under tensile testing was verified provided by the ABAQUS 2016 HTML Documentation (“Benchmarks Guide”, “Material Tests”, “Elasticity”, “Anisotropic hyper-elastic modelling of arterial layers”) as the maximum relative error of Cauchy stresses, Reaction Forces and Displacements was 2.6 %.

Appendix A.3

Subsequent to the development and verification of UMAT codes, the Strain Energy Density Function with energy limiter was implemented in the Fortran codes of Neo-Hookean and HGO material models. First, the Strain Energy Density Function (WE) was calculated and then, based on the damage loop, the “damaged” Strain Energy (WK) was formed and calculated for every element, increment or step of the analysis, as presented in the following [Table 5](#).

Table 5. Implementation of energy limiter in UMAT written in Fortran for Neo-Hookean and HGO material models.

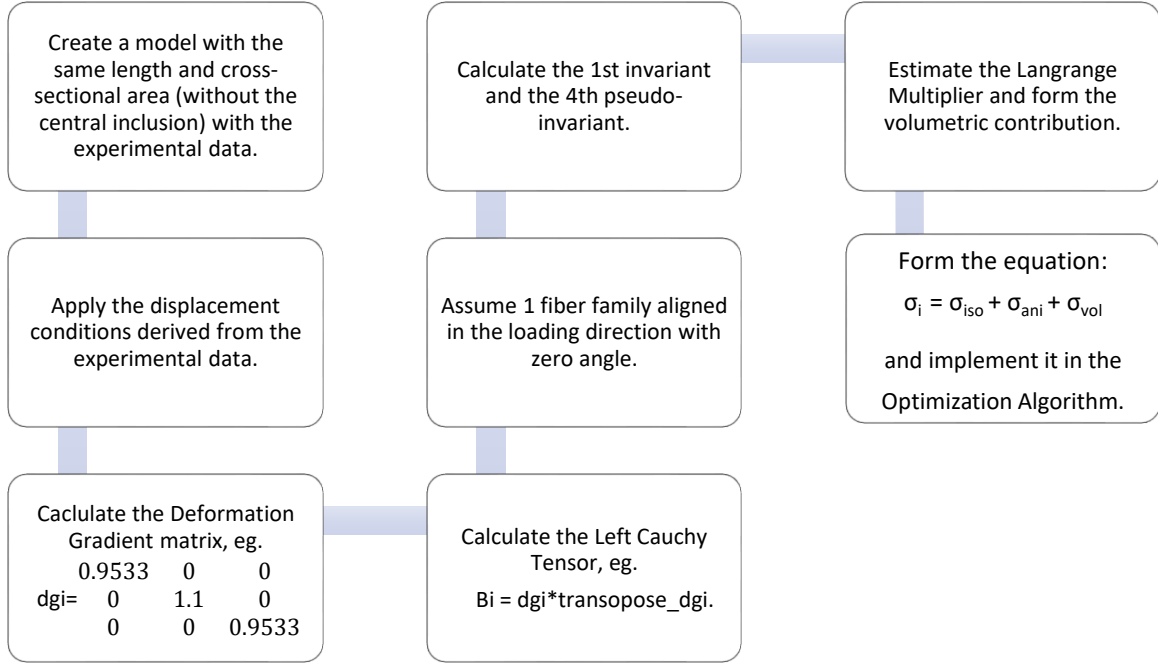
Neo- Hookean Model	<pre> %% Calculate the Strain Energy Density Function without damage (WE) and the E value (TK) WE = C10 * ((XB(1) + XB(2) + XB(3)) - THREE) + (ONE / XD1) * (XD - ONE)**2 C TK = SQRT(TWO * WE) %% Implement the damage loop – energy limiter (with $\beta_k = 0$) within crack initiation threshold (T1) and totally damaged threshold (T2) IF (TK .LT. T1) THEN DAM = ZERO ELSE IF (TK .GE. T1 .OR. TK .LE. T2) THEN DAM = ((TK - T1) / (T2 - T1))**TWO ELSE DAM = ONE END IF %% Calculate the Strain Energy Density Function with Energy Limiter (WK) and the reduction factor (1 - D) </pre>
--------------------	---

	<pre> WK = (ONE - DAM) * (C10 * ((XB(1) + XB(2) + XB(3)) - THREE) + (ONE /XD1) * (XD - ONE)**2) </pre>
	<pre> C RFACTOR = ONE - DAM </pre>
HGO Model	<pre> %% Calculate the Strain Energy Density Function without damage (WE) and the E value (TK) WE = C10*(I1 - 3.D0) + (k1/2.D0*k2)*(exp(EAA) - 1.D0) + (1.D0/D1)*(J**TWO - 1.D0)/2.D0 - LOG(J) </pre>
	<pre> C TK = SQRT(TWO * WE) %% Implement the damage loop - energy limiter (with $\beta_k = 0$) within crack initiation threshold (T1) and totally damaged threshold (T2) IF (TK .LT. T1) THEN DAM = ZERO ELSE IF (TK .GE. T1 .OR. TK .LE. T2) THEN DAM = ((TK - T1) / (T2 - T1))**TWO ELSE DAM = ONE END IF %% Calculate the Strain Energy Function with Energy Limiter (WK) and the reduction factor (1 - D) WK = (1.D0 - DAM)*(C10*(I1 - 3.D0) + (k1/2.D0*k2)*(exp(EAA) - 1.D0)) + (1.D0/D1)*(J**TWO - 1.D0)/2.D0 - LOG(J) </pre>
	<pre> C RFACTOR = ONE - DAM </pre>

Appendix B

In the material evaluation process of the HGO material model, an iterative optimization algorithm was generated via the MATLAB R2019a (MathWorks) and Wolfram Mathematica Notebook 12.0.0.0. All necessary steps are described through a schematic illustration in [Fig.10](#), regarding 20 different displacement conditions.

Fig.10. Flowchart of all required steps during the HGO material parameters estimation via a developed iterative optimization algorithm.



The hybrid formulation of the HGO model resulted in an additional calculation of the volumetric part in each of the 20 different displacement conditions of the initial experimental case without the central soft inclusion. The volumetric part or the hydrostatic stress consists of the Lagrange Multiplier $-p\mathbf{I}$, where p describes the equilibrium – boundary conditions (hydrostatic pressure) and \mathbf{I} is the identity matrix. The p value varied for every time point of the simulation (20 different time points) but was the same in all directions (xx' , yy' , zz') in every time point. As a result, the Lagrange Multiplier was the fifth unknown vector. In order to estimate the Lagrange Multiplier, Cauchy stress equations in “no-loading” directions (xx' , zz') were used, expressed by

$$\sigma_{xx} = 0 \rightarrow \sigma_{iso,x} + \sigma_{aniso,x} - p\mathbf{I} = 0 \rightarrow \sigma_{iso,x} + \sigma_{aniso,x} = p\mathbf{I} \quad (13)$$

$$\sigma_{zz} = 0 \rightarrow \sigma_{iso,z} + \sigma_{aniso,z} - p\mathbf{I} = 0 \rightarrow \sigma_{iso,z} + \sigma_{aniso,z} = p\mathbf{I} \quad (14)$$

$$\sigma_{iso} = \frac{2}{j} \cdot [C_{10} + e^{k_2 \cdot (\kappa(I_1-3) + (1-3\kappa) \cdot (I_4(\alpha\alpha)-1))} \cdot \kappa \cdot (\kappa(I_1-3) + (1-3\kappa) \cdot (I_4(\alpha\alpha)-1)) \cdot k_1] \cdot J^{2/3} \cdot (B - \frac{I_1}{3}) \quad (15)$$

$$\sigma_{aniso} = \frac{2}{j} \cdot [e^{k_2 \cdot (\kappa(I_1-3) + (1-3\kappa) \cdot (I_4(\alpha\alpha)-1))} \cdot (1-3\kappa) \cdot (\kappa(I_1-3) + (1-3\kappa) \cdot (I_4(\alpha\alpha)-1)) \cdot k_1] \cdot (m_i \cdot m_j - \frac{I_4(\alpha\alpha)}{3}) \quad (16)$$

In the x- and z-direction the fibre part contribution was eliminated ($\sigma_{aniso} = 0$) as the fibres were aligned in y-direction. A reference example of calculating the Lagrange Multiplier for the first of the 20 different displacement cases via the Wolfram Mathematica Notebook 12.0.0.0 by setting $x_1 = C_{10}$, $x_2 = k_1$, $x_3 = k_2$, $x_4 = \kappa$ (4 unknowns in the HGO material model) is presented as:

$$p\mathbf{I} = \sigma_{iso,x} \rightarrow p_1 = -2 \cdot (x_1 + E^{(x_3 \cdot ((0.3 \cdot x_4 - 0.0913)^2))} \cdot x_4 \cdot (0.3 \cdot x_4 - 0.0913) \cdot x_2) \cdot (1.21 - \frac{3.027}{3}) \quad (17)$$

During the final step of the optimization procedure, 20 different functions were created based on $\sigma_i = \sigma_{iso} + \sigma_{ani} + \sigma_{vol}$ formulation and after mathematical calculations the two algorithms of the overdetermined systems with 4 and 3 unknowns with $\kappa = 0.3333$ and $\kappa = 0$, respectively, are presented in the following MATLAB codes.

```

function F = material3(x)
F(1) = 0.004*(x(1) + exp(x(3)*((0.300*x(4) - 0.0913)^2))*x(4)*(0.300*x(4) +
0.0913)*x(2))+ 1.817/100*(exp(x(3)*((3/10*x(4)-9.13/100)^2))*(1 -
3*x(4))*0.300*x(4) + 0.0913)*x(2)) + 0.002*(x(1) + exp(x(3)*((0.300*x(4) -
0.0913)^2))*x(4)*(0.300*x(4) + 0.0913)*x(2))
F(2) = 0.0081*(x(1) + exp(x(3)*((0.303*x(4) - 0.0915)^2))*x(4)*(0.303*x(4) +
0.0915)*x(2)) + 0.03634*(exp(x(3)*((0.303*x(4) - 0.0915)^2))*(1 -
3*x(4))*0.303*x(4) + 0.0915)*x(2)) + 0.00404*(x(1) + exp(x(3)*((0.303*x(4) -
0.0915)^2))*x(4)*(0.303*x(4) + 0.0915)*x(2))
F(3) = 0.01215*(x(1) + exp(x(3)*((3.303/10*x(4) - 9.18/100)^2))*x(4)*(0.303*x(4) +
0.0918)*x(2)) + 0.05448*(exp(x(3)*((0.303*x(4) - 0.0918)^2))*(1 -
3*x(4))*0.303*x(4) + 0.0918)*x(2)) + 0.00606*(x(1) + exp(x(3)*((0.303*x(4) -
0.0918)^2))*x(4)*(0.303*x(4) + 0.0918)*x(2))
F(4) = 0.0162*(x(1) + exp(x(3)*((3.04/10*x(4) - 9.2/100)^2))*x(4)*(0.304*x(4) +
0.0920)*x(2))+7.264/100*(exp(x(3)*((3.04/10*x(4) - 9.20/100)^2))*(1 -
3*x(4))*0.304*x(4) + 0.0920)*x(2)) + 0.00808*(x(1) + exp(x(3)*((0.304*x(4) -
0.0920)^2))*x(4)*(0.304*x(4) + 0.0920)*x(2))
F(5) = 0.02045*(x(1) + exp(x(3)*((3.06/10*x(4) - 9.24/100)^2))*x(4)*(0.306*x(4) +
0.0924)*x(2)) + 0.09075*(exp(x(3)*((0.306*x(4) - 0.0924)^2))*(1 -
3*x(4))*0.306*x(4) + 0.0924)*x(2)) + 0.0102*(x(1) + exp(x(3)*((0.306*x(4) -
0.0924)^2))*x(4)*(0.306*x(4) + 0.0924)*x(2))
F(6) = 0.02454*(x(1) + exp(x(3)*((3.06/10*x(4) - 9.24/100)^2))*x(4)*(0.306*x(4) +
0.0924)*x(2)) + 0.1089*(exp(x(3)*((0.306*x(4) - 0.0924)^2))*(1 -
3*x(4))*0.306*x(4) + 0.0924)*x(2)) + 0.01224*(x(1) + exp(x(3)*((0.306*x(4) -
0.0924)^2))*x(4)*(0.306*x(4) + 0.0924)*x(2))
F(7) = 0.02863*(x(1) + exp(x(3)*((3.07/10*x(4) - 9.26/100)^2))*x(4)*(0.307*x(4) +
0.0926)*x(2)) +12.698/100*(exp(x(3)*((3.07/10*x(4) - 9.26/100)^2))*(1 -
3*x(4))*0.307*x(4) + 0.0926)*x(2)) + 0.01428*(x(1) + exp(x(3)*((0.307*x(4) -
0.0926)^2))*x(4)*(0.307*x(4) + 0.0926)*x(2))
F(8) = 0.03272*(x(1) + exp(x(3)*((3.07/10*x(4) - 9.28/100)^2))*x(4)*(0.307*x(4) +
0.0928)*x(2)) + 0.14512*(exp(x(3)*((0.307*x(4) - 0.0928)^2))*(1 -
3*x(4))*0.307*x(4) + 0.0928)*x(2)) + 0.01632*(x(1) + exp(x(3)*((0.307*x(4) -
0.0928)^2))*x(4)*(0.307*x(4) + 0.0928)*x(2))
F(9) = 0.03681*(x(1) + exp(x(3)*((3.07/10*x(4) - 9.28/100)^2))*x(4)*(0.307*x(4) +
0.0928)*x(2)) + 0.16317*(exp(x(3)*((0.307*x(4) - 0.0928)^2))*(1 -
3*x(4))*0.307*x(4) + 0.0928)*x(2)) + 0.01836*(x(1) + exp(x(3)*((0.307*x(4) -
0.0928)^2))*x(4)*(0.307*x(4) + 0.0928)*x(2))
F(10) = 0.04132*(x(1) + exp(x(3)*((3.09/10*x(4) - 9.32/100)^2))*x(4)*(0.309*x(4) +
0.0932)*x(2)) +18.13/100*(exp(x(3)*((3.09/10*x(4) - 9.32/100)^2))*(1 -
3*x(4))*0.309*x(4) + 0.0932)*x(2)) + 0.0206*(x(1) + exp(x(3)*((0.309*x(4) -
0.0932)^2))*x(4)*(0.309*x(4) + 0.0932)*x(2))
F(11) = 0.045452*(x(1) + exp(x(3)*((3.09/10*x(4) - 9.32/100)^2))*x(4)*(0.309*x(4) +
0.0932)*x(2)) + 0.19943*(exp(x(3)*((0.309*x(4) - 0.0932)^2))*(1 -
3*x(4))*0.309*x(4) + 0.0932)*x(2)) + 0.02266*(x(1) + exp(x(3)*((0.309*x(4) -
0.0932)^2))*x(4)*(0.309*x(4) + 0.0932)*x(2))
F(12) = 0.049584*(x(1) + exp(x(3)*((3.09/10*x(4) - 9.36/100)^2))*x(4)*(0.309*x(4) +
0.0934)*x(2)) + 0.21756*(exp(x(3)*((0.309*x(4) - 0.0936)^2))*(1 -
3*x(4))*0.309*x(4) + 0.0934)*x(2)) + 0.02472*(x(1) + exp(x(3)*((0.309*x(4) -
0.0934)^2))*x(4)*(0.309*x(4) + 0.0934)*x(2))
F(13) = 0.053716*(x(1) + exp(x(3)*((3.10/10*x(4) - 9.36/100)^2))*x(4)*(0.310*x(4) +
0.0936)*x(2)) + 23.569/100*(exp(x(3)*((3.10/10*x(4) - 9.36/100)^2))*(1 -
3*x(4))*0.310*x(4) + 0.0936)*x(2)) + 0.02678*(x(1) + exp(x(3)*((0.310*x(4) -
0.0936)^2))*x(4)*(0.310*x(4) + 0.0936)*x(2))
F(14) = 0.057848*(x(1) + exp(x(3)*((3.10/10*x(4) - 9.36/100)^2))*x(4)*(0.310*x(4) +
0.0936)*x(2)) + 0.25368*(exp(x(3)*((0.310*x(4) - 0.0936)^2))*(1 -
3*x(4))*0.310*x(4) + 0.0936)*x(2)) + 0.02884*(x(1) + exp(x(3)*((0.310*x(4) -
0.0936)^2))*x(4)*(0.310*x(4) + 0.0936)*x(2))
F(15) = 0.06198*(x(1) + exp(x(3)*((3.1/10*x(4) - 9.36/100)^2))*x(4)*(0.310*x(4) +
0.0936)*x(2)) + 0.2718*(exp(x(3)*((0.310*x(4) - 0.0936)^2))*(1 -
3*x(4))*0.310*x(4) + 0.0936)*x(2)) + 0.0309*(x(1) + exp(x(3)*((0.310*x(4) -
0.0936)^2))*x(4)*(0.310*x(4) + 0.0936)*x(2))
F(16) = 0.066112*(x(1) + exp(x(3)*((3.1/10*x(4) - 9.37/100)^2))*x(4)*(0.310*x(4) +
0.0937)*x(2)) + 28.992/100*(exp(x(3)*((3.1/10*x(4) - 9.37/100)^2))*(1 -
3*x(4))*0.310*x(4) + 0.0937)*x(2)) + 0.03296*(x(1) + exp(x(3)*((0.310*x(4) -
0.0937)^2))*x(4)*(0.310*x(4) + 0.0937)*x(2))
F(17) = 0.07089*(x(1) + exp(x(3)*((3.10/10*x(4) - 9.37/100)^2))*x(4)*(0.310*x(4) +
0.0937)*x(2)) + 0.30804*(exp(x(3)*((0.310*x(4) - 0.0937)^2))*(1 -

```

```

3*x(4))*(0.310*x(4) + 0.0937)*x(2)) + 0.03536*(x(1) + exp(x(3))*((0.310*x(4) -
0.0937)^2))*x(4)*(0.310*x(4) + 0.0937)*x(2))
F(18) = 0.07506*(x(1) + exp(x(3))*((3.12/10*x(4) - 9.39/100)^2))*x(4)*(0.312*x(4) +
0.0939)*x(2)) + 0.32616*(exp(x(3))*((0.312*x(4) - 0.0939)^2))*(1 -
3*x(4))*(0.312*x(4) + 0.0939)*x(2)) + 0.03744*(x(1) + exp(x(3))*((0.312*x(4) -
0.0939)^2))*x(4)*(0.312*x(4) + 0.0939)*x(2))
F(19) = 0.07923*(x(1) + exp(x(3))*((3.12/10*x(4) - 9.39/100)^2))*x(4)*(0.312*x(4) +
0.0939)*x(2)) + 34.428/100*(exp(x(3))*((3.12/10*x(4) - 9.39/100)^2))*(1 -
3*x(4))*(0.312*x(4) + 0.0939)*x(2)) + 0.03952*(x(1) + exp(x(3))*((0.312*x(4) -
0.0939)^2))*x(4)*(0.312*x(4) + 0.0939)*x(2))
F(20) = 0.0834*(x(1) + exp(x(3))*((3.12/10*x(4) - 9.41/100)^2))*x(4)*(0.312*x(4) +
0.0941)*x(2)) + 0.3622*(exp(x(3))*((0.312*x(4) - 0.0941)^2))*(1 -
3*x(4))*(0.312*x(4) + 0.0941)*x(2)) + 0.0416*(x(1) + exp(x(3))*((0.312*x(4) -
0.0941)^2))*x(4)*(0.312*x(4) + 0.0941)*x(2))

%% Optimization Process
lb = [0,0,0,0];
ub = [inf,inf,inf,0.333];
rng default;
options.Algorithm = 'trust-region-reflective';
options.Display = 'final-detailed';
options.TolFun = 0.000001;
options.TolX = 0.000001;
options.MaxFunEvals = 1000;
options.MaxIter = 400;
options.FunValCheck = 'on';
options.PlotFcns = 'optimplotfval';
x0 = randi([0,100],4,1);
[x,resnorm,residual,exitflag,output] = lsqnonlin(@material3,x0,lb,ub,options)

function F = material33(x)
F(1) = 0.004*x(1)+0.01817*(exp(x(3))*((0.0913)^2))*(+0.0913)*x(2))+ 0.002*x(1)
F(2) = 0.0081*x(1)+0.03634*(exp(x(3))*((0.0915)^2))*(+0.0915)*x(2))+ 0.00404*x(1)
F(3) = 0.01215*x(1)+0.05448*(exp(x(3))*((0.0918)^2))*(+0.0918)*x(2))+ 0.00606*x(1)
F(4) = 0.0162*x(1)+0.07264*(exp(x(3))*((0.0920)^2))*(+0.0920)*x(2))+ 0.00808*x(1)
F(5) = 0.02045*x(1)+0.09075*(exp(x(3))*((0.0924)^2))*(+0.0924)*x(2))+ 0.0102*x(1)
F(6) = 0.02454*x(1)+0.1089*(exp(x(3))*((0.0924)^2))*(+0.0924)*x(2))+ 0.01224*x(1)
F(7) = 0.02863*x(1)+0.12698*(exp(x(3))*((0.0926)^2))*(+0.0926)*x(2))+ 0.01428*x(1)
F(8) = 0.03272*x(1)+0.14512*(exp(x(3))*((0.0928)^2))*(+0.0928)*x(2))+ 0.01632*x(1)
F(9) = 0.03681*x(1)+0.16317*(exp(x(3))*((0.0928)^2))*(+0.0928)*x(2))+ 0.01836*x(1)
F(10) = 0.04132*x(1)+0.1813*(exp(x(3))*((0.0932)^2))*(+0.0932)*x(2))+ 0.0206*x(1)
F(11) = 0.045452*x(1)+0.19943*(exp(x(3))*((0.0932)^2))*(+0.0932)*x(2)+ 0.02266*x(1)
F(12) = 0.049584*x(1)+0.21756*(exp(x(3))*((0.0936)^2))*(+0.0934)*x(2))+ 0.02472*x(1)
F(13) = 0.053716*x(1)+0.23569*(exp(x(3))*((0.0936)^2))*(+0.0936)*x(2))+ 0.02678*x(1)
F(14) = 0.057848*x(1)+0.25368*(exp(x(3))*((0.0936)^2))*(+0.0936)*x(2))+ 0.02884*x(1)
F(15) = 0.06198*x(1)+0.2718*(exp(x(3))*((0.0936)^2))*(+0.0936)*x(2))+ 0.0309*x(1)
F(16) = 0.066112*x(1)+0.28992*(exp(x(3))*((0.0937)^2))*(+0.0937)*x(2))+ 0.03296*x(1)
F(17) = 0.07089*x(1)+0.30804*(exp(x(3))*((0.0937)^2))*(+0.0937)*x(2))+ 0.03536*x(1)
F(18) = 0.07506*x(1)+0.32616*(exp(x(3))*((0.0939)^2))*(+0.0939)*x(2))+ 0.03744*x(1)
F(19) = 0.07923*x(1)+0.34428*(exp(x(3))*((0.0939)^2))*(+0.0939)*x(2))+ 0.03952*x(1)
F(20) = 0.0834*x(1)+0.3622*(exp(x(3))*((0.0941)^2))*(+0.0941)*x(2))+ 0.0416*x(1)

%% Optimization Process
lb = [0,0,0];
ub = [inf,inf,inf];
rng default;
options.Algorithm = 'trust-region-reflective';
options.Display = 'final-detailed';
options.TolFun = 0.000001;
options.TolX = 0.000001;
options.MaxFunEvals = 1000;
options.MaxIter = 400;
options.FunValCheck = 'on';
options.PlotFcns = 'optimplotfval';
x0 = randi([0,100],3,1);
[x,resnorm,residual,exitflag,output] = lsqnonlin(@material33,x0,lb,ub,options)

```

According to the results of the iterative optimization algorithm, both HGO material models fitted well the experimental data, as presented in [Fig.11](#). During the calculation of the relative errors the HGO models with $\kappa= 0.333$ and $\kappa= 0$ resulted in 20% and 29% average relative errors, respectively.

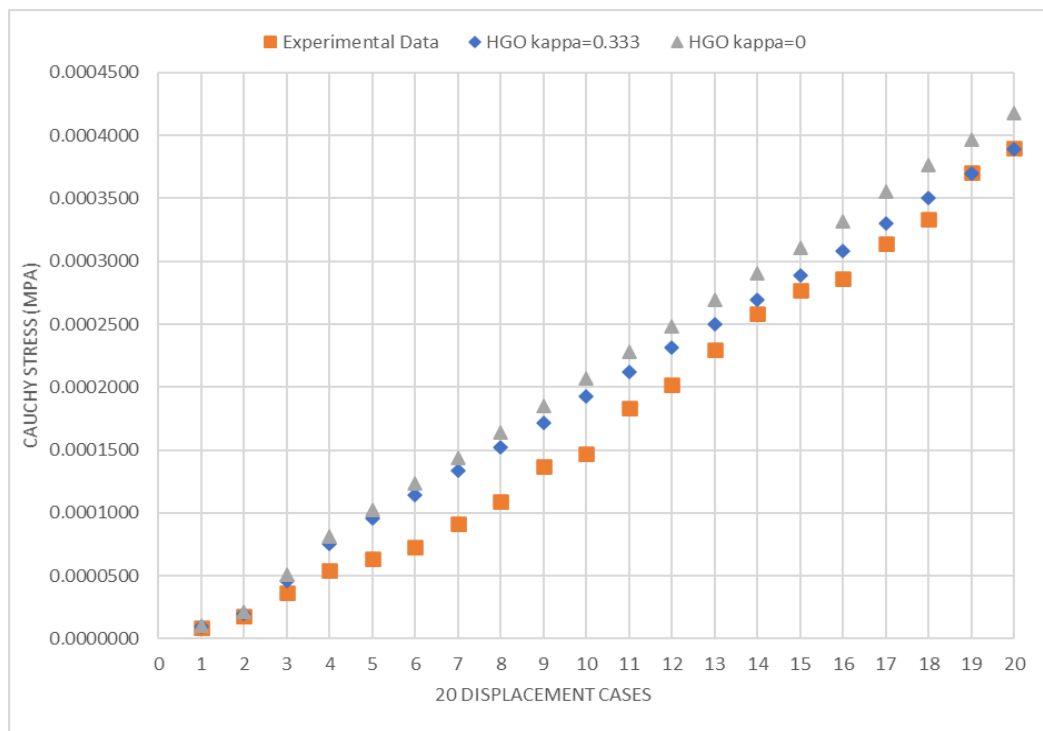


Fig. 11. The Cauchy stress values of all 20 displacement cases regarding the experimental data and the HGO material model with $\kappa = 0$ and 0.333 after the iterative optimization procedure.

Appendix C

Table 6. The separate matrix and fibers SEDF with energy limiter calculations and reduction factors via HGO UMAT code.

```

HGO Material      %% Calculate the Matrix Strain Energy Function (XWE1) and the  $\bar{\epsilon}_m$  value (TK1)
Model
XWE1 = C10*(XI1 - 3.D0)
TK1 = SQRT(TWO * XWE1)

%% The Matrix damage loop – Implement the energy limiter (with  $\beta_k = 0$ ) within
crack initiation threshold (T2M) and totally damaged threshold (T3) and the
reduction factor (1 – D)

IF (TK1 .LT. T2M) THEN
  DAM1 = ZERO
ELSE IF (TK1 .GE. T2M .OR. TK1 .LE. T3) THEN
  DAM1 = ((TK1 - T2M) / (T3 - T2M))**TWO
ELSE
  DAM1 = ONE
END IF
C
RF1 = ONE - DAM1

%% Calculate the Fibres Strain Energy Function (XWE2) and the  $\bar{\epsilon}_f$  value (TK2)

XWE2 = (xk1/2.D0*xk2)*((exp(EAA)) - 1.D0)
TK2 = SQRT(TWO * XWE2)

%% The Fibres damage loop – Implement the energy limiter (with  $\beta_k = 0$ ) within
crack initiation threshold (T2) and totally damaged threshold (T3) and the
reduction factor (1 – D)

IF (TK2 .LT. T2F) THEN
  DAM2 = ZERO
ELSE IF (TK2 .GE. T2F .OR. TK2 .LE. T3) THEN
  DAM2 = ((TK2 - T2F) / (T3 - T2F))**TWO
ELSE
  DAM2 = ONE
END IF
C
RF2 = ONE - DAM2

```

Appendix D

The crack initiation and propagation were simulated by element deletion option, via post-processing analysis (“Visualization”, “Status Variable”) in ABAQUS 2016 (Dassault Systems), depicted in [Tables 7, 8, 9, 10](#). When the SEDF of the elements reached the implemented energy limiter, the elements were automatically deleted. The reason why Gradient Damage, Phase-Field approach or X-FEM were not implemented as damage models, in order to illustrate the element separation, was the lack of pre-defined crack path, the applied elements were not linear elastic and the implemented crack thresholds were energy-based and not stress-based.

Table 7. Crack initiation comparison between experimental data and Ideal computational models, where variable SDV7,8 is the Strain Energy Density Function with energy limiter distribution.

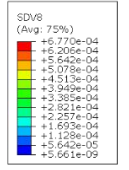
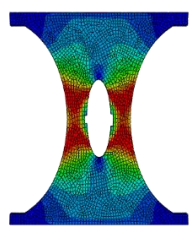
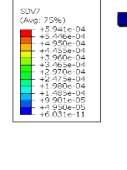
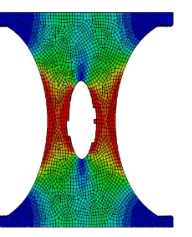
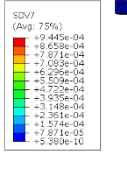
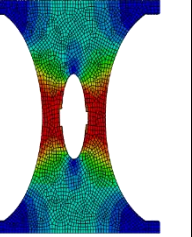
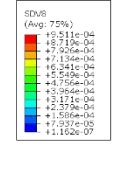
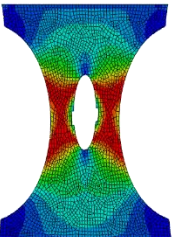
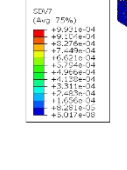
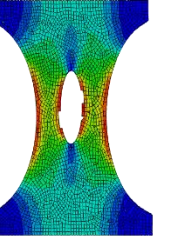
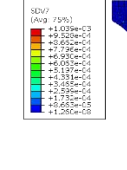
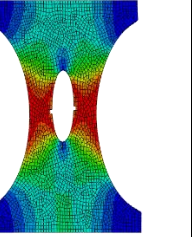
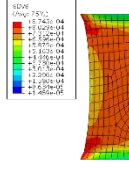
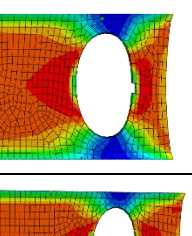
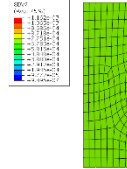
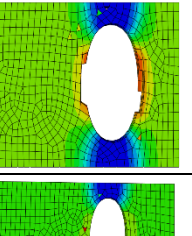
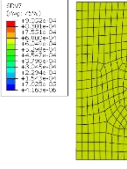
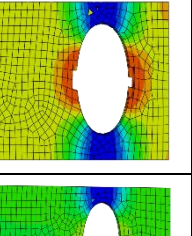
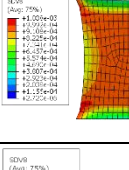
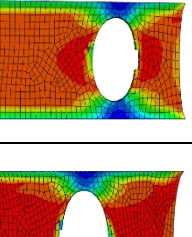
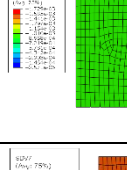
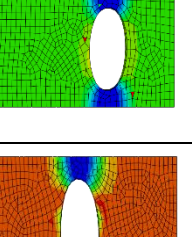
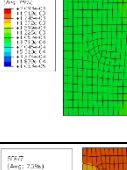
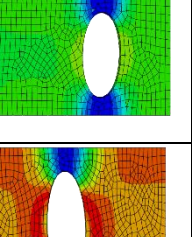
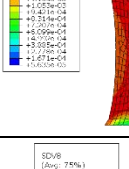
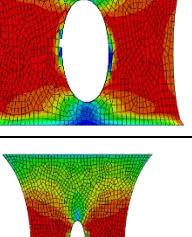
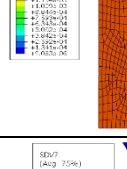
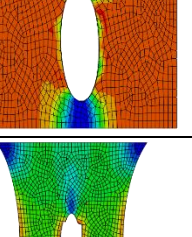
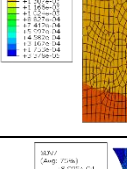
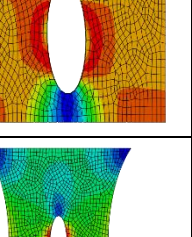
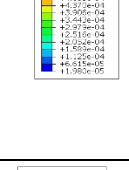
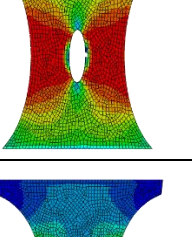
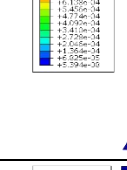
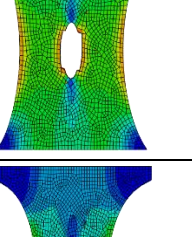
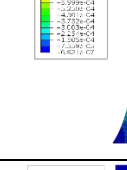
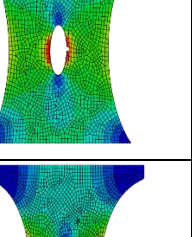
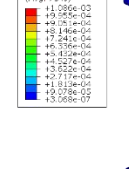
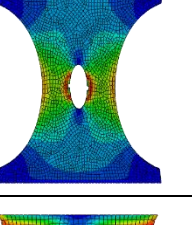
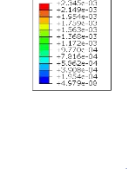
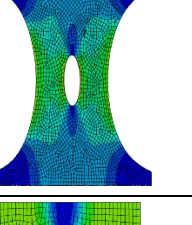
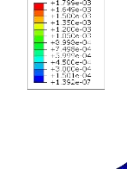
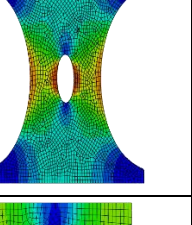
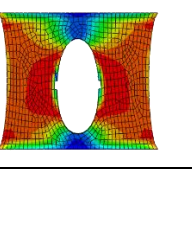
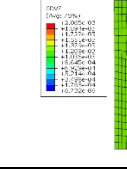
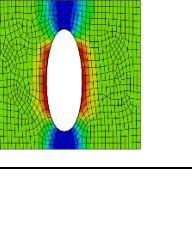
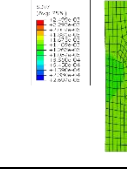
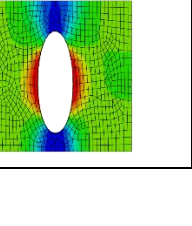
	Ideal Models		
	Neo-Hookean	HGO _{aniso}	HGO _{iso}
1	 	 	 
2	 	 	 
3	 	 	 
4	 	 	 
5	 	 	 
6	 	 	 
7	 	 	 
8	 	 	 

Table 8. Crack initiation comparison between experimental data and Image-based computational models, where variable SDV7,8 is the Strain Energy Density Function with energy limiter distribution.

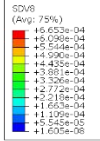
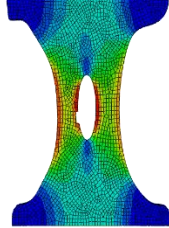
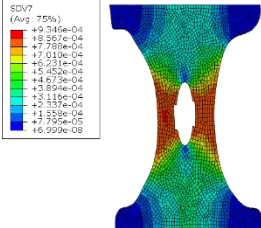
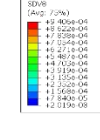
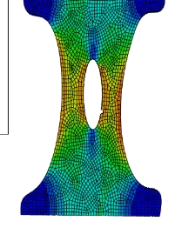
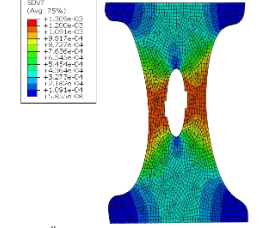
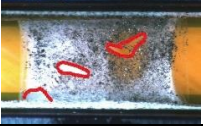
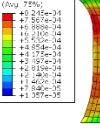
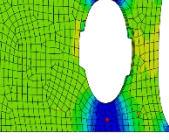
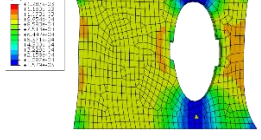
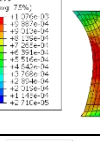
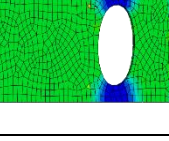
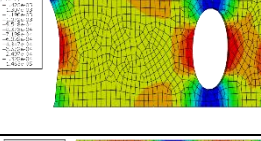
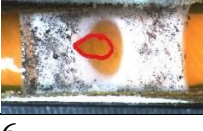
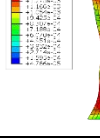
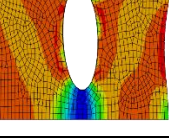
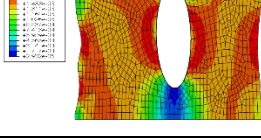
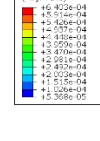
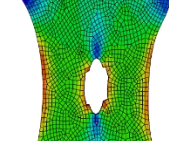
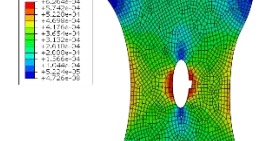
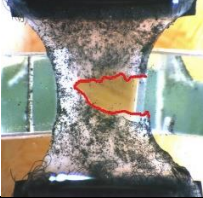
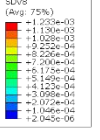
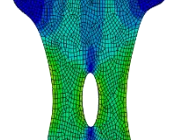
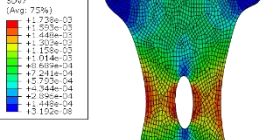
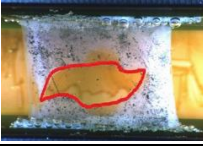
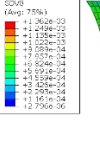
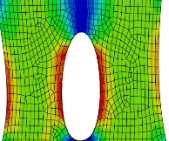
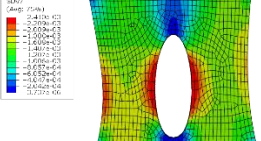
	Image-based Models		
	Neo-Hookean	HGO _{aniso}	HGO _{iso}
1	   		
2	   		
3	   		
4	   		
5	   		
6	   		
7	   		
8	   		

Table 9. Crack propagation comparison between experimental data and Ideal computational models, where variable SDV7,8 is the Strain Energy Density Function with energy limiter distribution.

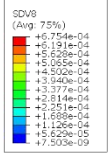
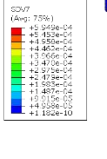
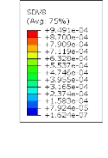
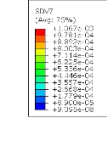
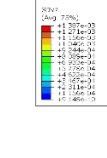
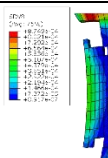
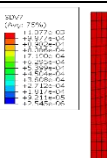
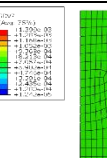
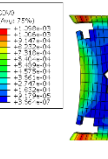
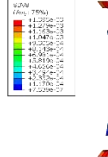
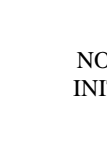
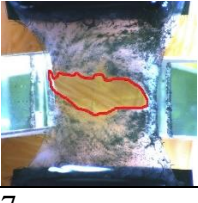
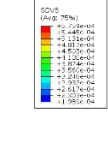
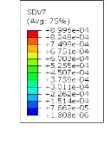
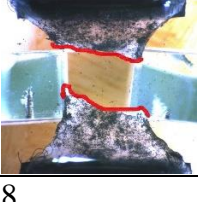
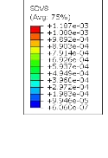
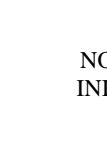
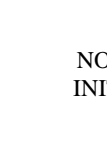
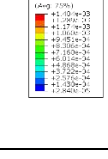
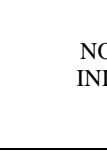
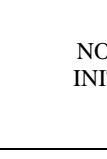
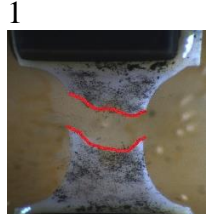
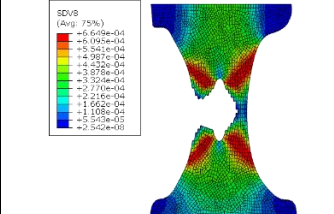
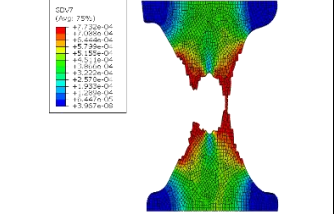
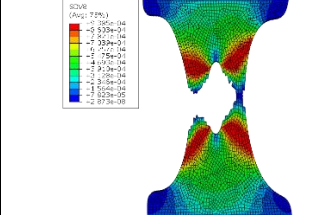
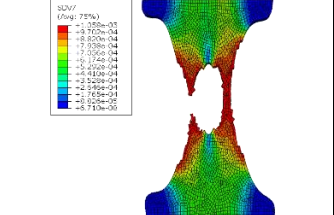
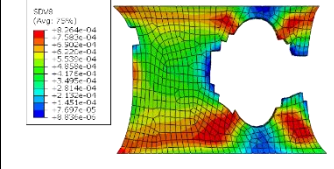
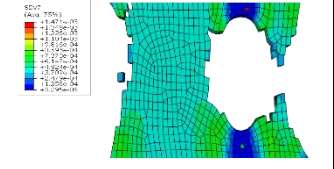
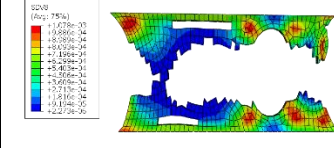
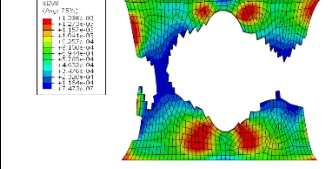
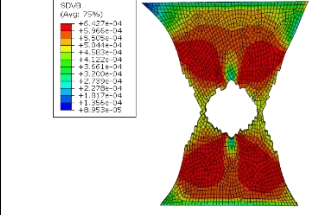
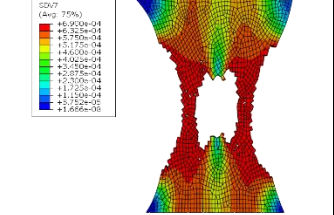
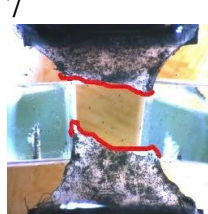
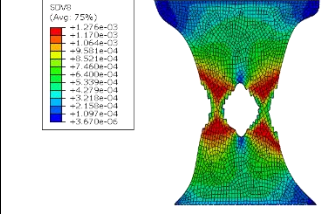
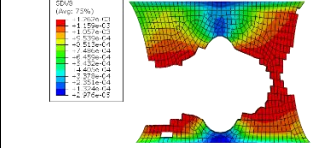
	Ideal Models		
	Neo-Hookean	HGO _{aniso}	HGO _{iso}
1	   		
2	   		
3	   		
4	   		
5	   		
6	   		
7	   		
8	   		

Table 10. Crack propagation comparison between experimental data and Image- based computational models, where variable SDV7,8 is the Strain Energy Density Function with energy limiter distribution.

	Image- based Models		
	Neo-Hookean	HGO _{aniso}	HGO _{iso}
1			
2			
3			
4			NO CRACK INITIATION
5			NO CRACK INITIATION
6			
7			NO CRACK INITIATION
8			NO CRACK INITIATION

Appendix E

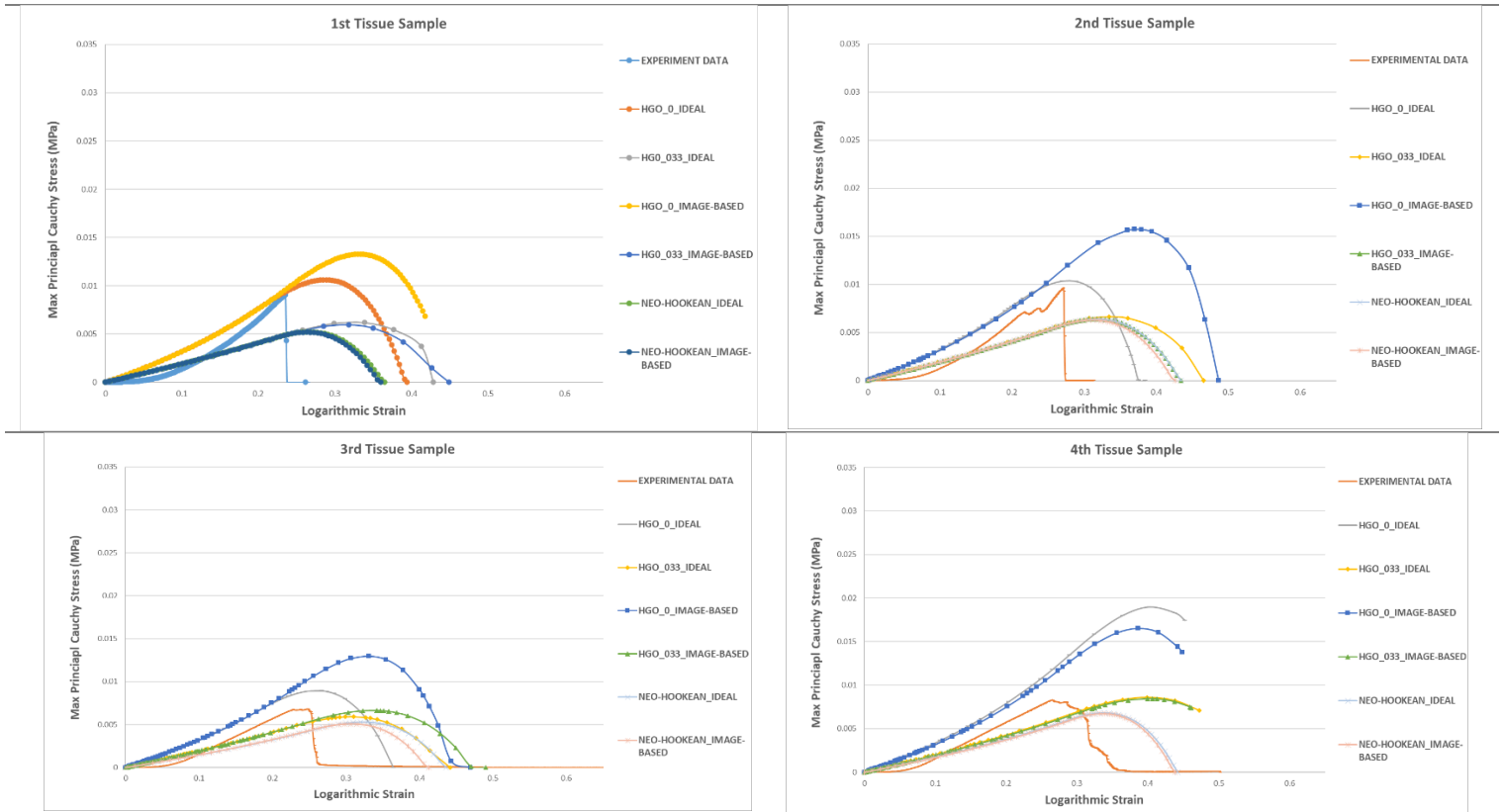
In the quantitative results, shown in Fig. 12, the experimental force data converted into Cauchy stresses as they were divided by the middle cross-sectional area (without the inclusion). Furthermore, the experimental displacement data transformed into logarithmic strain divided by the total tissue length in y- direction and followed the equation:

$$\text{logarithmic Strain} = \ln(1 + \text{engineering Strain}) \quad (18)$$

The Cauchy stresses and the logarithmic strain in the middle cross-sectional area of the computational simulations were calculated by finite element software ABAQUS 2016 (Dassault Systems). However, due to the fact that the damage loop of the energy limiter affected only the calculated Strain Energy function, the “damaged” Cauchy stresses were estimated according to the following equation:

$$\sigma_{\text{dam}} = (1 - D) * \sigma_{\text{ini}}^0 \quad (19)$$

where σ_{dam} is the Cauchy stress including the implemented energy limiter, (1- D) is the reduction factor calculated for every element, time increment or frame and σ_{ini}^0 is the initial Cauchy stress without the applied damage model.



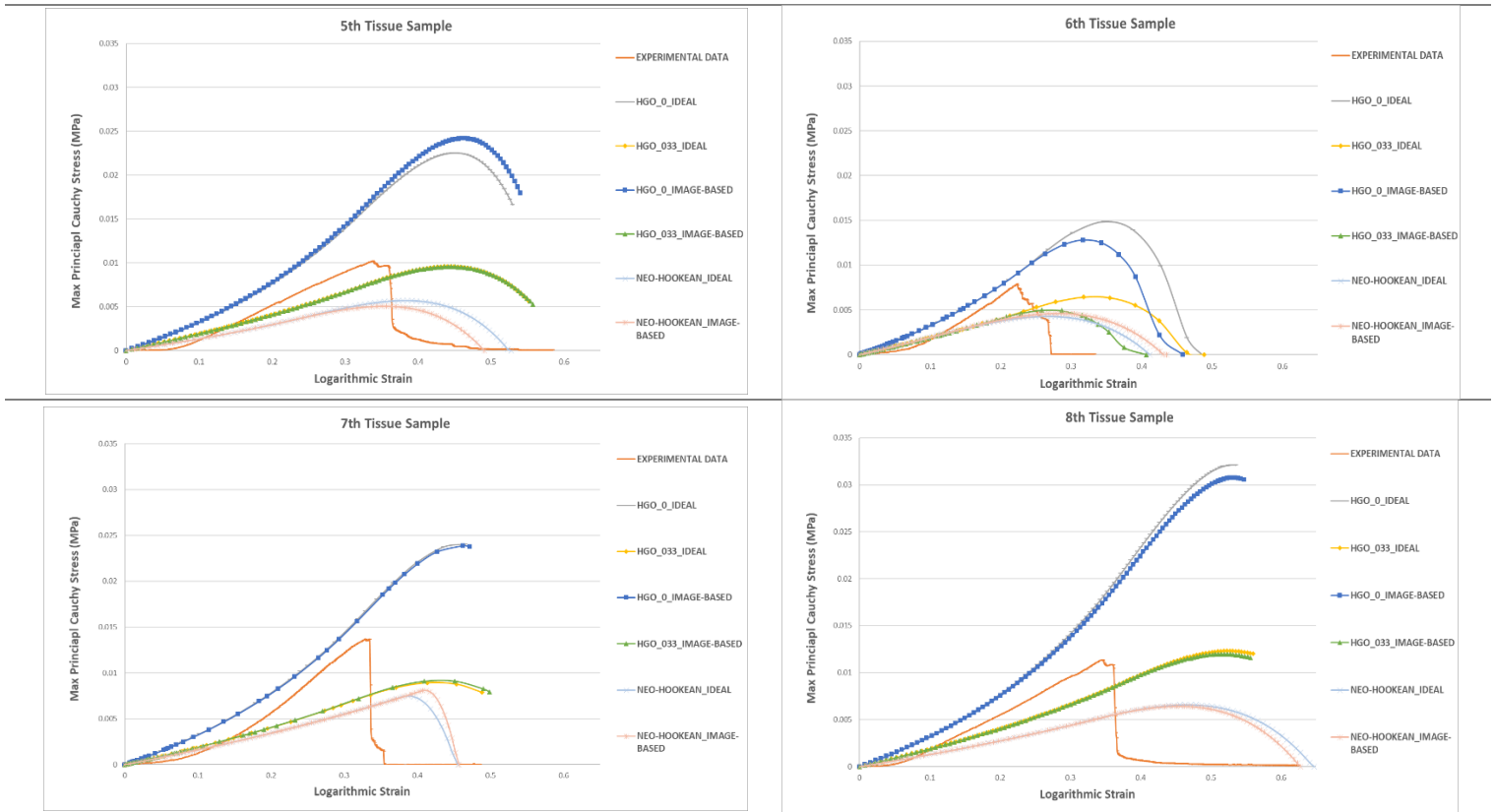
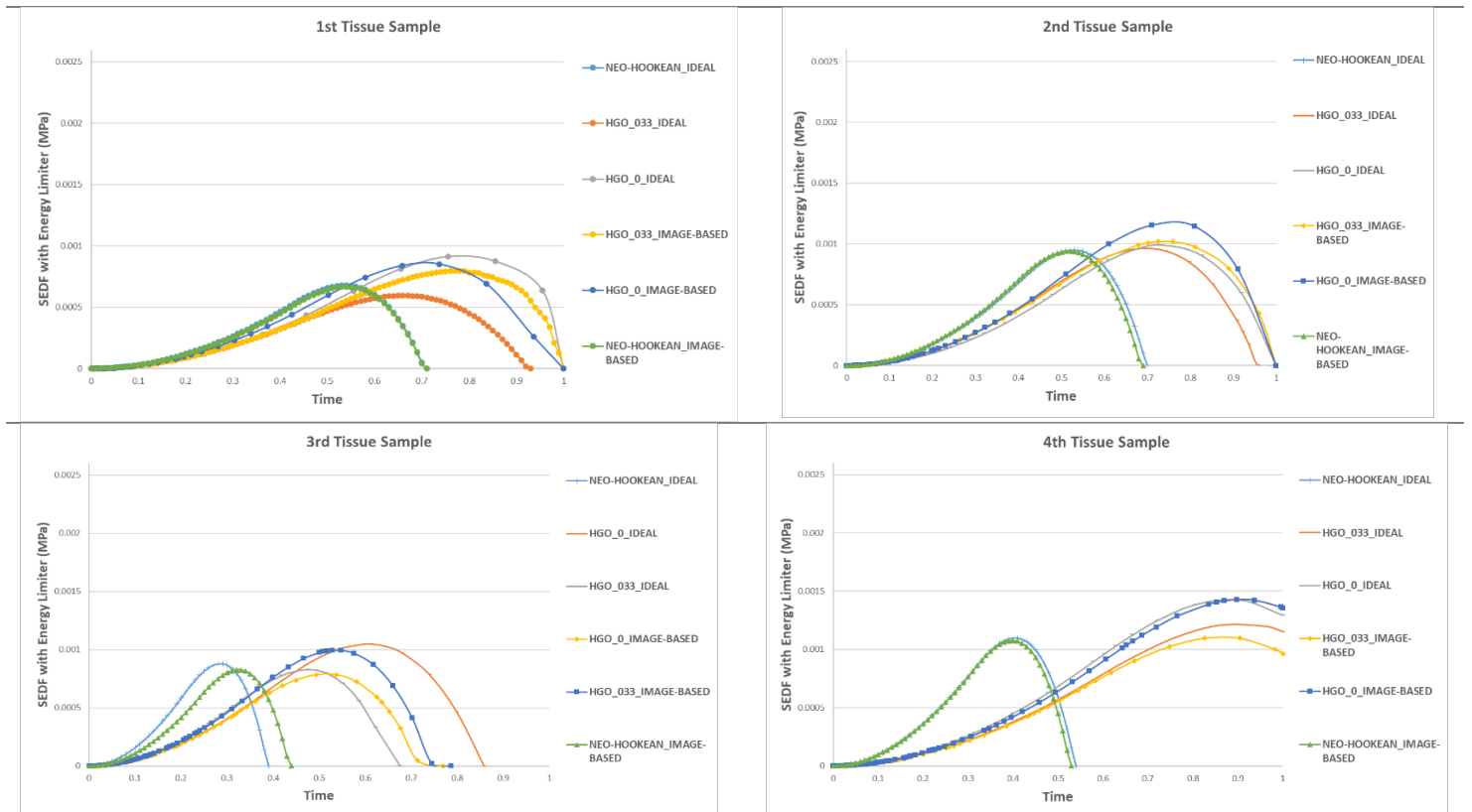


Fig. 12. Quantitative comparison of Maximum Principal Cauchy Stress vs Logarithmic Strain of the first damaged element between experimental data and computational models following the SEDF with energy limiter damage model.



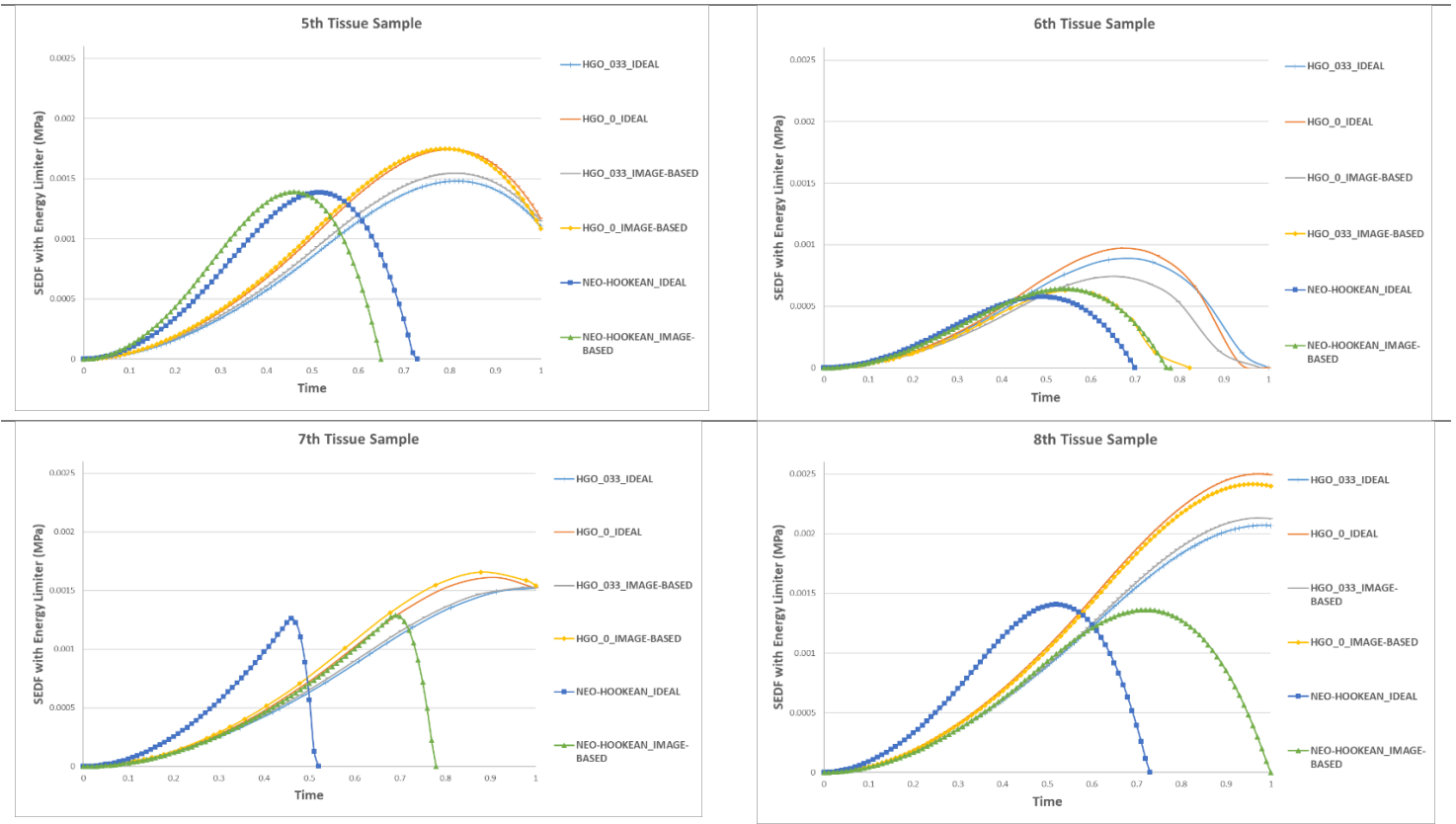


Fig. 13. Quantitative comparison of Strain Energy Density Function with energy limiter vs Time of the first damaged element between computational models of Neo-Hookean and HGO.